Journal of Physics D: Applied Physics

PAPER • **OPEN ACCESS**

Metal vapor content of an electric arc initiated by exploding wire in a model N_2 circuit breaker: simulation and experiment

To cite this article: A Kadivar *et al* 2021 *J. Phys. D: Appl. Phys.* **54** 055203

OPEN ACCESS
IOP Publishing
Journal of Physics D: Applied Physics
J. Phys. D: Appl. Phys. **54** (2021) 055203 (20pp)
https://doi.org/10.1088/1361-6463/abba92

Metal vapor content of an electric arc initiated by exploding wire in a model N_2 circuit breaker: simulation and experiment

A Kadivar[1,2], K Niayesh[1], N Sasaki Støa-Aanensen[3] and F Abid[1]

[1] Department of Electric Power Engineering, NTNU, Trondheim, Norway
[2] Department of Transmission Line and Substation Equipment, Niroo Research Institute (NRI), Tehran, Iran
[3] Department of Electric Power Technology, SINTEF Energy Research, Trondheim, Norway

E-mail: ali.kadivar@ntnu.no

Received 12 June 2020, revised 26 August 2020
Accepted for publication 22 September 2020
Published 10 November 2020

Abstract

A conductive wire can explode by rapidly heating it to vaporization temperature by flowing a current through it. This process is utilized to generate high-temperature high-density plasmas. The temperature and pressure distributions at the time of the explosion are not easily measured. Moreover, the amount of metal vapor from the wire that remains within the arcing area is unknown. This work presents the whole-process model of a single-wire electrical explosion from solid-state to plasma formation. For this purpose, the voltage drop and resistance of the exploding copper wire in solid-state are simulated through a zero-dimensional thermo-electrical model. Then, compressible Euler equations are implemented with nodal discontinuous Lagrange shape functions in a one-dimensional model to compute the flow of the generated copper vapor (due to the wire explosion) in surrounding nitrogen gas. The aim is to calculate the distributions of pressure, density, velocity, temperature, and mass flow along the cylindrical shock waves to estimate the arc's copper/nitrogen mixture ratio in free burning and nozzle constricted arcs. This mixture ratio is used to calculate the precise percentage of the metal vapor in the arcing area and to calculate Townsend growth coefficients utilizing to estimate the streamer breakdown of the mixture. The simulation results show good agreement with the experimental results in terms of the temporal evolution of the plasma channel boundary, the shock front speed estimation as well as the arc voltage magnitude numerically calculated deploying the extracted mixture percentage from this study, manifesting the validity of the model. It shows that despite the low-pressure studies, the exploding wire method is not suitable for circuit breakers employing supercritical fluids as the insulation.

Keywords: high-Mach-number flows, shock waves, supercritical fluids, whole-process model, single-wire electrical explosion, plasma formation

(Some figures may appear in colour only in the online journal)

1. Introduction

An electric explosion of a thin metal wire (characteristic diameter $\approx$ 20–50 μm) (EEW) [1] constitutes a sharp change of the conductor state by an intensive energy input that leads

to lattice destruction, phase transitions, generation of shock waves (SW) and electromagnetic radiation. The end-products of the exploding wire process (EWP) are metal vapor and powders [2]. SWs have a crucial role in heating, ionizing, and spreading the plasma particles including metal vapor generated from exploding wire or ablated from electrode contacts in a hot plasma. EWP is encountered in the fields of particle beams, high-power lasers, radiation sources, pulsed magnetic fields, and applications include circuit breakers (CB), segmented lightning diverter strips for aircraft radomes, disruption of metallic shaped charge jets, plasma armatures for electromagnetic railguns and plasma generators for electrothermal–chemical guns [3].

A time-transient code for analyzing copper wire explosion driven by a slow current rise in a pressure vessel filled with nitrogen is developed. At first, an initial voltage drop over the copper wire, current, and temperature distribution at the time of explosion as well as changes in wire resistance are derived. Data from this 'first stage' are then used as the initial conditions of a second stage, in which a simplified one-dimensional (1D) model for high-Mach-number flows (HMaNF) is adopted. The adopted model describes the expansion speed of the vaporized wire to estimate the arc's copper/nitrogen mixture ratio for different filling pressures and wire diameters. The effects of the metal wire diameter have been studied by others experimentally [4] but not through the simulations. In the third stage, using a three-dimensional (3D) model, the streamer threshold is estimated based on the calculated copper/nitrogen mixture.

1.1. Guide to the study

A disadvantage of utilizing EEW in the study of CBs [5], is injecting an enormous amount of metal vapor into the electric arc plasma that will affect all the transport properties needed in the magneto-hydrodynamic (MHD) simulations of the arc [6]. The radiation as a function of arc temperature, T, is the most important cooling mechanism of the arc which is very sensitive to the metal vapor content [7]. Even small percentages of metal vapor at the arc temperature range (15 000 K–25 000 K) can significantly affect its radiative level, the energy balance of the arc, and consequently, its voltage magnitude [8].

Utilizing the ideal gas equations alone to calculate the molar ratio of the mixture results in unrealistic estimations that do not fit with measurements from experiments. This can be explained by the SW effects as it will disperse the metal vapor inside the arcing area but the higher filling pressure results in the lower dispersing ability and therefore, the higher mixture ratio in the arc column.

A general method for investigating the metal vapor content in an electrically initiated plasma was presented and verified by experiments. Other numerical simulations of the initial plasma formation (PF) in vacuum [9] or underwater [10] are also available. Still, to the authors' knowledge, the method for the calculation of the mixture ratio in high-pressure gases and supercritical fluids (SCFs) presented in this paper has not been published by other researchers so far. This method is believed

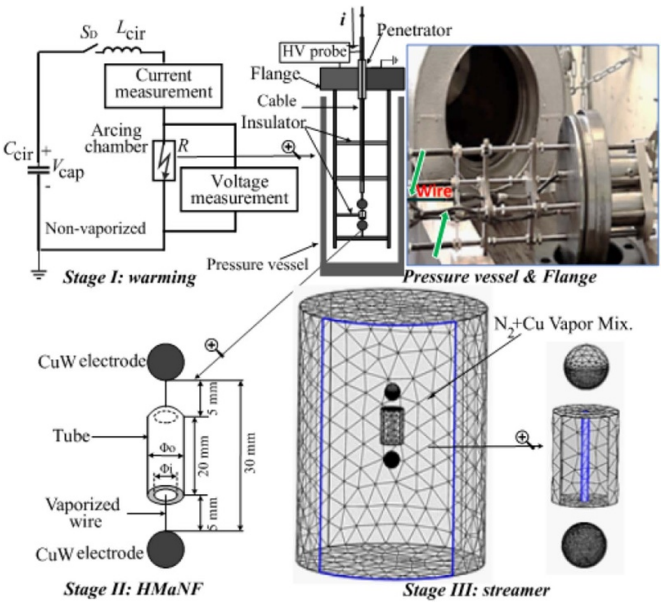

Figure 1. Schematics of the test circuit at each of three stages; the high-pressure arcing chamber and flange, and 3D geometry for the simulation of streamer breakdown inside the cylindrical nozzle.

to be useful for the study of high-pressure plasmas for example in the study of current interruption in SCF and the simulation studies of replacing the greenhouse SF_6 gas where almost all environmentally friendly alternatives shall be used in a pressure higher than what SF_6 was utilized at.

Figure 1 shows the schematics of the setup including the high-pressure arcing chamber, the inside connections together with a 25 μm tick copper wire inside the cylindrical nozzle, and the 3D geometry for the simulation of streamer breakdown. A pressure vessel of 15.7 liter rated for 500 bar is used as the arcing chamber. When the knife switch, S_D, is closed, the capacitor, C_{cir}, is discharged through the inductor, L_{cir}, which fed the ignition wire through the cable passing a penetrator inside the screwed flange (the techniques for this setup are described in [11]). The return path of the current, i, is through the metal body of the vessel. An HV probe is utilized to measure the voltage across the electrodes and a shunt resistor is used for the current measurement. The exploding wire and the nozzle are fixed through insulating supports. Then the flange is screwed to the vessel.

As mentioned in the introduction, the process of the single-wire electrical explosion (and this paper structure) is divided into three stages: stage (I) warming; the wire is in the non-vaporized state, stage (II) HMaNF; the vaporized wire starts to expand, and stage (III) streamer; the breakdown in the gas mixture of N_2 + Cu vapor occurs. The thermodynamic calculation is applied before the wire melts completely in stage I. In stage II, a 1D computational fluid dynamics (CFD) model comes into play until the instant that voltage collapse occurs. The temperature, density, and velocity, which are derived from the CFD calculation, are averaged over the arcing area. These three stages are not separated and overlap with each other.

The averaged parameters are taken as the initial conditions for stage III in which a simplified streamer model based on the Schumann criterion is applied in 3D to the gas mixture. Experiments with the same setup as simulated in the model were carried out, and the voltage drop and current magnitude across the exploding wire in the test bench were measured. Moreover, the velocity of the SW is estimated based on the delay between power (P) and voltage (V) peaks and compared with the simulation results. Fast imaging was not utilized but it is available for similar wires in another research [3].

2. Voltage drop development on the wire (stage I)

2.1. Electro-thermodynamic calculation

The governing equation for the electrical circuit shown in figure 1 containing an exploding wire at intermediate frequencies (f < 20 MHz) is derived based on a generalized form of Kirchhoff's voltage law as zero-dimensional (0D) model, where the resistance ($R_{\rm cir}$) is variable due to the change in ignition wire resistance, R, but the inductance ($L_{\rm cir}$) and capacitance ($C_{\rm cir}$) are fixed:

$$\frac{d^2 i}{dt^2} + \frac{R_{cir}}{L_{cir}} \cdot \frac{di}{dt} + \frac{1}{L_{cir} \cdot C_{cir}} \cdot i = 0. \tag{1}$$

Due to the fast heating, the thermal expansion of the wire and convection are neglected and heat conduction is merged in radiation. So, we can write:

$$R_{cir} \cdot i^2 - \frac{dQ_{rad}(T)}{dT} \frac{dT}{dt}\, m_{wire} \left(\left[C_V(T) + T. \frac{dC_V(T)}{dT} \right] \cdot \frac{dT}{dt} - LH_{melt}.\delta\left(T - T_m(p)\right) - LH_{vap}.\delta\left(T - T_V(p)\right) = 0, \right. \tag{2}$$

$$R_{cir} = R(T, state) + R_{connectors}, \tag{3}$$

$$R(T, state) = \frac{L_{wire}}{\sigma(T).S_{wire}(t)} = \frac{L_{wire}^2}{m_{wire}(t)} \cdot \frac{\rho(T)}{\sigma(T)}. \tag{4}$$

δ is the Dirac delta function. (1) is solved for current $i(t)$, and (2) is solved for temperature $T(t)$. Q_{rad} is the radiated energy from the exploding wire. $m_{\rm wire}$, $S_{\rm wire}$, $L_{\rm wire}$, σ and ρ are the mass, cross section, length, electric conductivity and mass density of the wire, respectively. $LH_{\rm melt}$, $LH_{\rm vap}$, T_m and T_v are latent heat of melting, latent heat of vaporization, melting temperature and evaporation temperature for copper, respectively. The latter two quantities are assumed to be pressure (p) dependent. Here, the inductance and capacitance are 43 mH and 4.8 μF. The initial conditions are $i(0) = 0$, $T(0) = 300$ and $di(0)/dt = -V_{cap}/L_{cir}$, where $V_{\rm cap}$ is the capacitor voltage. The current frequency in the experiment is about 352 Hz. The skin depth is larger than the radius of the concerned ignition copper wires, i.e. uniform current distribution was assumed. The calculation starts from a solid-state without additional estimated or measured parameters. The circuit equation, equations (1) and (2) are coupled with the electrical resistance of the circuit shown in (3) and (4) including the connectors, $R_{\rm connectors}$, and the resistance of the ignition copper wire, R, which is a function of its physical state, temperature and the remained mass of the wire, $m_{\rm wire}(t)$. The $m_{\rm wire}(t)$ is calculated through (5) based on the $\rho(x,T)$ from solving Euler equations in stage II. The latent heat of melting and vaporization, as well as the step changes in R at transition points, are considered in the simulation through thermodynamic calculation [12].

$$m_{\rm wire}(t) = 2\pi \cdot L_{\rm wire} \cdot \int_{x=0}^{x=D} x\rho(x,T)\,{\rm d}x. \tag{5}$$

Here, $i(t), T(t), R(t)$ and $Q_{rad}(t)$ are functions of time but for easy writing the time dependency is not shown in the equation except for the m_{wire} in (5). The other functions used in (2) are as mentioned here below in equations (6)–(15):

$$T_V(p) = \frac{15850}{5.55 + \log\left(p_{amb} + p_{Mag} + p_{preburst}\right)}. \tag{6}$$

The dependency of melting temperature, $T_m(p)$, to the pressure is weak but the vaporization temperature, $T_V(p)$, is a function of the surrounding pressure, p, which consists of three components, the ambient pressure, p_{amb}, magnetic pressure, p_{Mag}, and the pre-burst pressure, $p_{preburst}$. An estimation of $T_V(p)$ for copper, shown in (6), is based on the method explained in [13] and the data in [14]:

$$p_{Mag} = 3 \times 10^{-14} \cdot J_{wire}^2 \cdot D_{wire}^2. \tag{7}$$

p_{Mag} according to [13] has two components, one is magnetic pinch effect and the other is due to the forces generated when the liquid expands against its magnetic field. The average of the two mentioned components is shown in (7). J_{wire} is the current density at pre-burst in A cm^{-2} and D_{wire} is the wire diameter in mil just here. $J_{wire} = 5.36 \times 10^6$ A cm^{-2} and $D_{wire} =$ 0.984 mil in this case, which (7) results in 0.834 bar overpressure but $p_{preburst}$ has an emormous value and is calculated by solving Euler equations in stage II.

$$Q_{rad}(T) = radii \cdot \frac{m_{wire}(t)}{\rho(T)}. \tag{8}$$

Heat conduction can also be expressed directly as an energy (loss) source term. So, the equivalent heat conductivity (thc_{tot}) due to radiation is calculated and is merged in the net emission coefficient (NEC) radiation shown as *radii* in (8), which is the NEC eestimation of the radiative cooling in W, through PLASIMO® code [15], which provides a better estimation than others [10]. $Q_{rad}(T)$ is in W. Heat capacity at constant volume, mass density and electrical conductivity of wire in different physical states are defined through (9)–(15):

$$C_V(T) = C_V(T)_{solid} + C_V(T)_{liquid} + C_V(p,T)_{gas}, \tag{9}$$

$$\rho(T) = \rho(T)_{solid} + \rho(T)_{liquid} + \rho(p,T)_{gas}, \tag{10}$$

$$\sigma(T) = \sigma(T)_{solid} + \sigma(T)_{liquid} + \sigma(p.T)_{gas}. \tag{11}$$

$C_V(T)_{solid}$ and $C_V(T)_{liquid}$ are defined in [16,17]. Equations (12) and (13) for $\rho(T)_{solid}$, and $\rho(T)_{liquid}$ are from [18] and (14) and (15) for $\sigma(T)_{solid}$, and $\sigma(T)_{liquid}$ are from [12]:

$$\rho(T)_{solid} = 8985 - 0.598 \cdot (T - 293)\,, \tag{12}$$

$$\rho(T)_{liquid} = \left(9077 - 8.006 \times 10^{-1} \cdot T\right), \tag{13}$$

$$\sigma(T)_{solid} = 5.88 \times 10^{7} - 4.52 \times 10^{4} \cdot (T - 293)\,, \tag{14}$$

$$\sigma(T)_{liquid} = 5.26 \times 10^{6} - 4.0 \times 10^{3} \cdot (T - 1370)\,. \tag{15}$$

PLASIMO® [15] is used to calculate the $C_V(p,T)_{gas}$, $\rho(p,T)_{gas}$, and $\sigma(p.T)_{gas}$ at p. Figure 2(a) shows simulated V and R considering the NEC, $V_{sim.\ with\ NEC}$ and $R_{sim.\ with\ NEC}$, versus measured ones, $V_{Meas.}$ and R_{Meas}.

The brown dots represent the measured current, $I_{Meas.\ points}$.

A practical method widely used in power signal processing especially for protection matters from 90s [19–21] to denoise signals with low signal to noise ratio (SNR) is discrete wavelet transform (DWT). Daubechies is the most popular wavelets for the detection of short duration, fast decaying oscillations [22, 23]. Daubechies-4 DWT (db4) in level 5 is utilized here to denoise $I_{Meas.\ points}$. The result, $I_{denoised}$, indicates that most of the oscillations are not due to noise or low sampling resolution; rather it is because of the change in R. It is clear from figure 2(a) that the current at the start of the EWP ($t = 76$ μs) is abruptly reduced and the simulation confirms this.

Simulations considering radiative cooling show good agreement with the experiments in the first 76–77 μs. Then, the V, i, and R suddenly change. Changes in wire temperature in figure 2(b) show the vaporization temperature is considerably higher (around 4800–5200 K) than the usually known vaporization temperature of copper at standard atmosphere (2835 K) or even at 1.83 atm due to the magnetic preessure effect (3000 K); as the dominant pressure at the outer conducting radius is the vapor pressure of the material. At high temperatures where vaporization is significant, the surface of the conductor is surrounded by a non-conducting vapor, and a two-phase thermodynamic system is created, where liquid and vapor coexist [24]. Thus, the vaporization occurs in saturated vapor pressure. Vaporization reduces the conducting part of the melted wire according to (5) and therefore R, and consequently, V are increased sharply until the arc plasma is created by the streamer in the mixture of nitrogen and copper vapor. This abrupt change in simulated signals in figure 2(a) is evident. The resistivity for most of the metals increases by a factor of two when they are melted [13] and this factor for the copper is about 2.07 [25] which is also clear from (14) and (15). This abrupt change is utilized to find the melting point from measured values to verify the calculations. Measurements show the melting has happened at around 65–75 μs which confirms the simulation results. Changes in the heat capacity, electrical conductivity, and mass density of 25 μm copper wire surrounded by 1 bar N_2 during the warming stage from solid to the gas state are shown in figures 2(c) and (d).

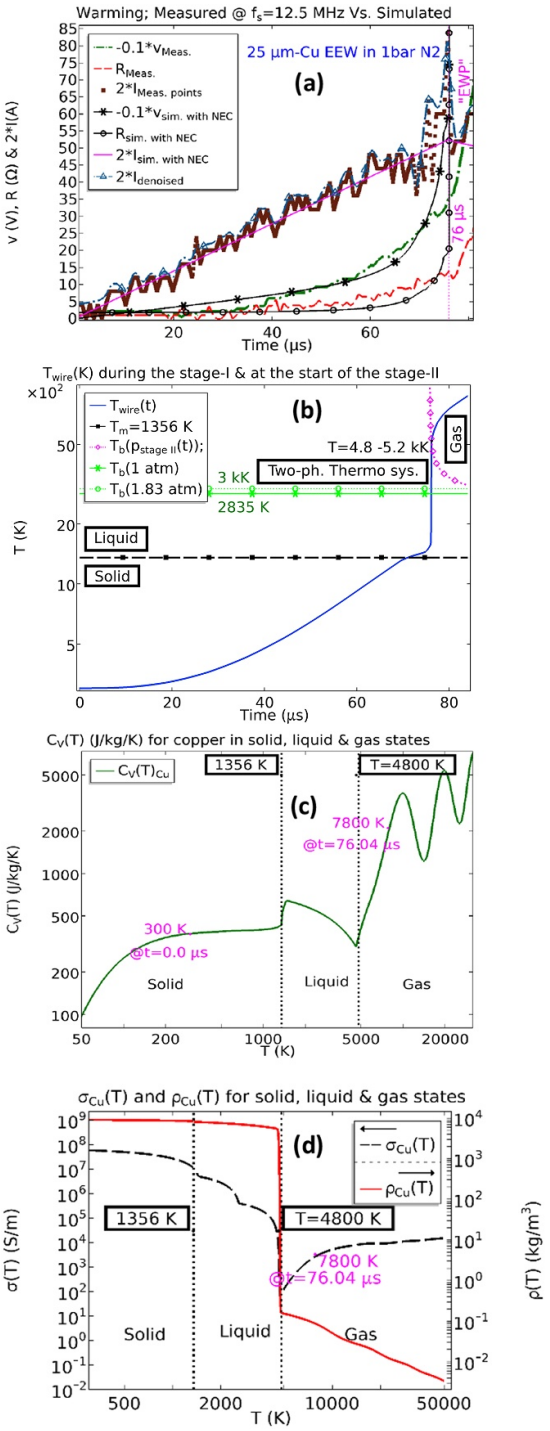

Figure 2. (a) Simulated voltage, current, and resistance versus measured ones, change in (b) T, (c) $C_V(T)$, (d) $\sigma(T)$ and $\rho(T)$ of 25 μm copper wire during warming stage at 1 bar N_2 from solid to gas state.

2.2. Scaled resistance function

It has been known for many years that the instantaneous resistance of an exploding wire is not a unique function of the energy deposited in the wire up to that instant [26]. This 'resistance anomaly' guides to present a measure named 'scaled

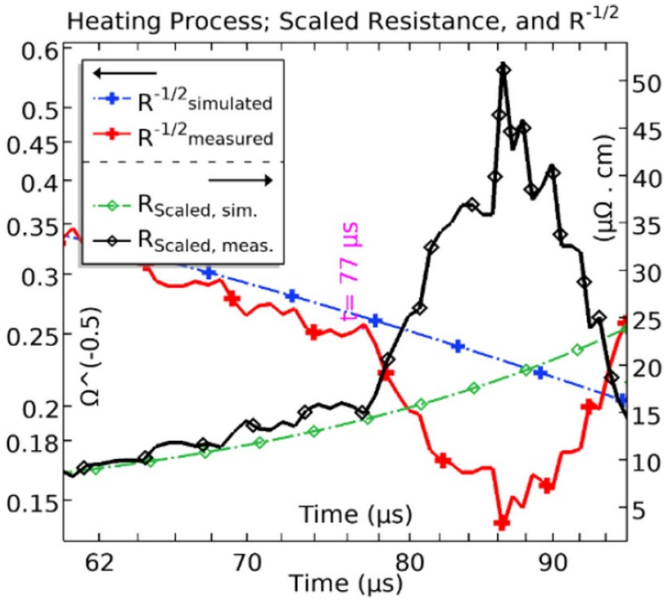

Figure 3. Scaled resistance and $R^{-1/2}$ versus simulated ones in 1 bar for 25 μm copper EEW.

resistance' which is defined as measured or simulated resistance of wire multiplied by its primary cross-section divided by its length (it is not the known linear resistivity). Plots of 'scaled resistance' versus time give a universal curve, for different wire sizes of the same material with similar energy densities [26]. Another parameter taken as an indication for the start of EWP is $R^{-1/2}$. Figure 3 shows measured scaled resistance and $R^{-1/2}$ for the explosion of 25 μm copper wire in 1 bar N_2 and its deviation from simulated ones at 76–77 μs where expansion starts. The peak of scaled resistance is 53 $\mu\Omega$cm that is in agreement with another study [24].

3. Shock wave expansion, HMaNF (stage II)

Our previous experimental work [27] has shown that even with different copper ignition wire diameters (25, 40, and 100 μm), the arcing voltage a few hundred microseconds after the explosion is almost equal in all three cases. It should be noted that delays and magnitudes for the initial voltage peak during the EWP are different (see e.g. figure 20). Another observation is seen for 25 μm thick wires, both for different filling pressures and at the presence of a nozzle with different inner diameters (see e.g. figure 22): Although the initial voltage peak delays are the same, the voltage magnitudes during the EWP are different. The abrupt change in the rate of resistance increment is taken as an indication of a sharp decrease in conducting cross-section. It means an SW is created that spreads the copper vapor inside the pressure vessel towards the nozzle wall and beyond the electrode region.

The following section will investigate this phenomenon by calculating the percentage of the metal vapor in the arcing area after the explosion through the simulation of HMaNFs around EEW where the SW is generated. Previous experimental works have demonstrated that wires remain rather uniform lengthwise during the explosion and can be simulated utilizing 1D simulations [28]. A 1D numerical model for the experimental setup presented in [27] is generated based on the equations for HMaNF (Mach number (Ma) > 1) coupled with the van-der-Waals (vdW) equation and is solved for different wire diameters and pressures as well as different nozzle diameters.

3.1. High-Mach number flow equations

Flow equations consist of compressible Euler equations (CEE) for mass, momentum, and energy. In equations (16)–(19), ρ is the mass density, u is the velocity, p is the pressure. x represents the radial distance from the wire (D_{radial}) or the distance from the wire to the nozzle's inner wall (R_{radial}) in the simulation results. γ is the ratio of the specific heats, and ε is the wire energy density:

$$\partial\rho/\partial t+\partial\left(\rho u\right)/\partial x=0, \tag{16}$$

$$\partial\left(\rho u\right)/\partial t+\partial\left(\rho u^2+p\right)/\partial x=0, \tag{17}$$

$$\partial\varepsilon/\partial t+\partial\left(\left(\varepsilon+p\right)u\right)/\partial x=0, \tag{18}$$

$$\varepsilon=p/\left(\gamma-1\right)+\frac{1}{2}\rho u^2. \tag{19}$$

The vdW equation of state for non-ideal gas, equations (20)–(25), together with the ideal gas relation equation (16) are utilized for the nitrogen mixed with copper vapor:

$$T_{N_2}R_{const}n=\left(p+n^2a/v^2\right)\left(v-nb\right), \tag{20}$$

$$a=\sum_{i=1}^{m}\sum_{j=1}^{m}\left(x_i,x_j\right)\sqrt{a_ia_j}, \tag{21}$$

$$b=\sum_{i=1}^{m}\sum_{j=1}^{m}\left(x_i,x_j\right)\sqrt{b_ib_j}, \tag{22}$$

$$a_{N_2}=0.139\ \&\ b_{N_2}=3.913\times10^{-5}, \tag{23}$$

$$b=\left(\frac{4}{3}\pi r_w^3+\pi r_w^2d\right)N_A, \tag{24}$$

$$d_{N_2}=1.0975A^0;\ r_{w\_N_2}=2.25A^0. \tag{25}$$

Here, pressure, p, the absolute temperature, T, the inter-nuclear distance, d [29] and the vdW radius r_w [30], are involved in (23), respectively. N_A is the Avogadro constant, n is the number of moles. a and b depend on the particular gas and V is

the volume, a $\left[\frac{m^3.atm}{mole^2}\right]$ is a measure of the average attraction between particles, and b $\left[\frac{m^3}{mole}\right]$ is the volume excluded by a mole of particles and is extracted from [29] for N_2. R_{const} is the universal constant of gases. The coefficients a and b for the mixture of m different gasses can be calculated from molar fractions of mixture elements, $x_{i,j}$ according to (24) and (25) [31];.

$$c^2 = \gamma R_{const} T. \tag{26}$$

Here, T and c are temperature and the speed of sound in the medium, respectively. Equations (27) and (28) show the stored energy in the capacitor, W_{in}, calculated by capacitor size, C_{cir}, and voltage, V_{cap}, and the wire energy density, ε defined as injected energy to the exploding wire per its volume, Vol_{wire},

$$W_{in} = \frac{1}{2} C_{cir} V_{cap}^2, \tag{27}$$

$$\varepsilon = V_{wire} \cdot i / Vol_{wire}. \tag{28}$$

The molar mass ratio of the mixture in percent at the time of the gas breakdown (voltage peak) and PF inside the arcing area, $X_{mixture}\%$, is calculated through the Dumas method in (32) from the calculated density, ρ_{calc} based on flow equations and the initial densities of elements:

$$X_{mixture}\% = 100\left(\rho_{calc} - \rho_{N_2}\right) / \left(\rho_{Cu} - \rho_{N_2}\right). \tag{29}$$

The wire diameter affects ρ and ε, and a change in nitrogen filling pressure affects the initial p and ε in flow equations that results in a change in the velocity u. Consequently, the size of the wire and the filling pressure can affect the density distribution. Moreover, the SW will be reflected after crossing the nozzle's inner wall and exhausts the gas inside the nozzle tube. The effects of the nozzle, wire diameter, and filling pressure on the calculated density, ρ_{calc}, are studied through simulations of the SWs' radial expansion.

3.1.1. Effects of wire diameter. The radial distances of the first and the second SW from the wire at any given time are simulated to investigate the waves' expansion like what typical Schlieren photos may show in general. The simulated area is 30 mm wide and divided into 3000 mesh elements in COMSOL® with a size of 10 μm. The time step is 180 ps at the start, then increased to 700 ps at the end of the simulation. Figure 4 shows the 'Schlieren-like' representation of the simulated velocity and *Ma* for the explosion of a 25 μm thick Cu-wire in 1 bar nitrogen exposed to sinusoidal 150 A current starting at zero. The current during the time of the wire explosion is a lot lower than 150 A, and it varies from 26.3 to 49.8 and 145 A for different wire diameters. An experiment with a pulse current for a wire explosion in the air was published elsewhere [32].

The simulated motion of the main SW, the formation, and subsequent motion of the secondary shock, as well as the location of the contact surface (CS) between the detonation gases and the outside atmosphere, are presented in figure 4, shows similarities with the general shape of the photographs from an experiment of an EEW in the atmosphere [33].

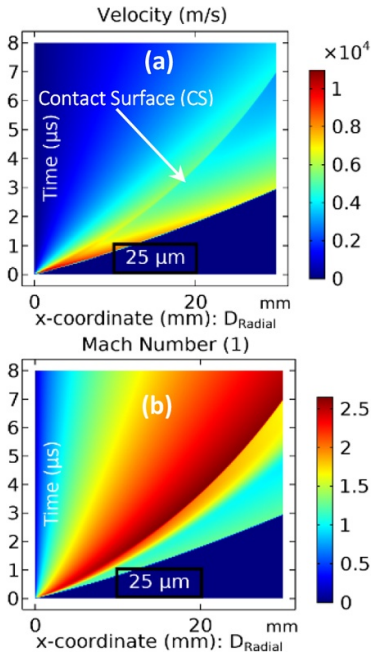

Figure 4. Schlieren-like representation of (a) velocity, and (b) Mach number in the explosion of 25 μm Cu wire at 1 bar N_2.

The time-tagged curves of the shock velocity up to 8 μs with the envelope of the front velocity ($U_{\text{w max}}$) over the simulated domain are shown in figure 5. The location of the CS and the motion of the shock can be identified from the small and then huge fluctuations in the velocity curves. The legend is similar for each case study and is showed one time per case. The front of an expansion wave propagating into undisturbed medium travels with the maximum velocity, $U_{\text{w max}}$. Here, the *Ma* and the wave velocity reach 2.5 and 11 000 m s^{-1}, respectively (see figures 4(b) and 5).

Figure 6(a) shows the simulated temperature wave through the 'Schlieren-like' representation and explains that the high-temperature part of the medium is in the main wave. Therefore, the temperature gradient is very high at the CS. Figure 6(b) shows the time-tagged curves of the temperature up to 8 μs after the explosion of a 25 μm thick copper wire, i.e. at the time when streamer breakdown takes place. The results agree with other studies, see e.g. [34]. The SW significantly contributes to plasma heating and initiation of the electrical arc. Measurements have shown that the warming stage before expansion depends on wire diameter [27], and radiation plays an important role in such long warming times at the temperature range of figure 6(b). Figures 7 and 8 show the distribution of density and pressure in the SW where the pressure in the GPa-range is observed. This pressure explains the higher vaporization temperature than the boiling point of copper. The average arc radius in free-burning (FB) arcs (i.e. inside the vessel but without nozzle) for the same geometry and electrode distances, like what is shown in figure 1, is calculated to be around 7.5 mm through a verified MHD model

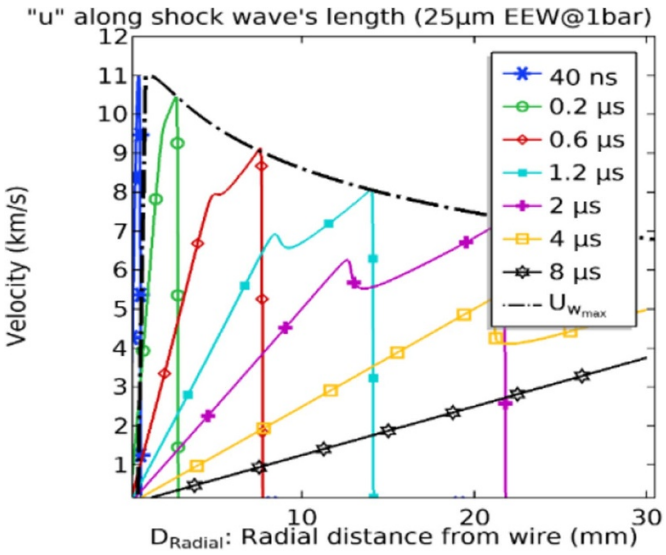

Figure 5. Simulated shock velocity and the envelope of the wave-front velocity for 25 μm copper wire explosion at 1 bar N_2.

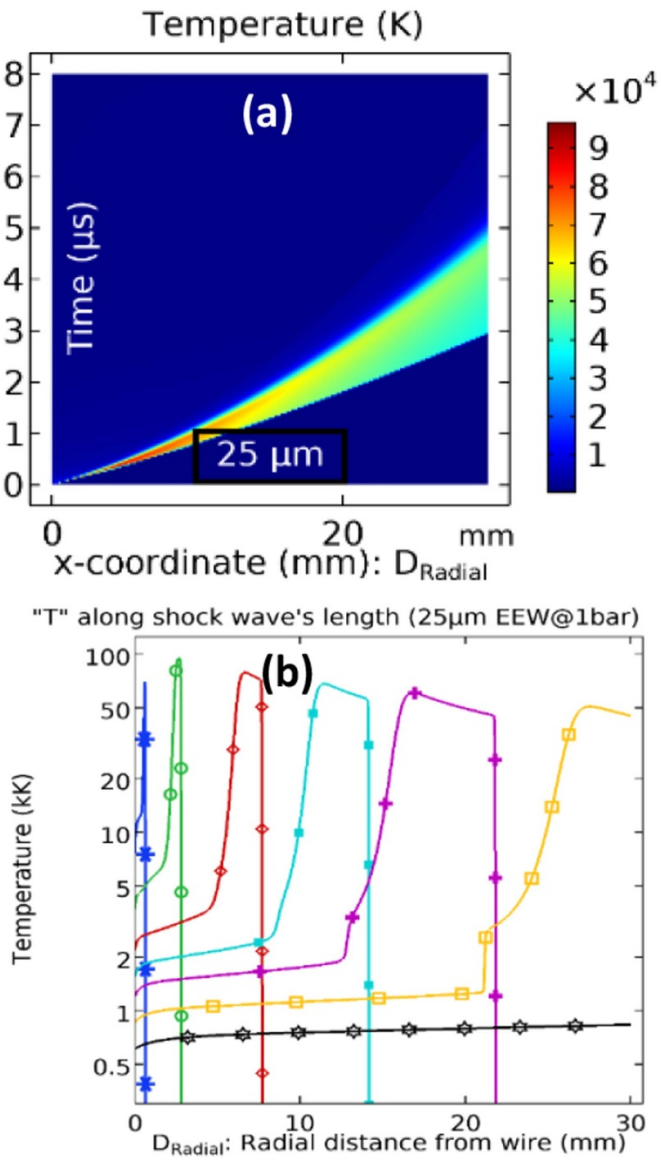

Figure 6. (a) Schlieren-like representation of temperature wave and (b) time-tagged curves of temperature for 25 μm wire case at 1 bar N_2 (the legend and time-taggings are like figure 5).

[35] in the N_2-Cu mixture and is shown here as the arc outer wall (AOW) in figures 7(a) and 8(a).

The simulated area in the mentioned MHD model was 15 mm but in axisymmetrical coordinates. A current of 145–150 A with a frequency of 352 Hz is applied and the conductivity contour of 500 S m^{-1} which is equal to 6000 K is considered as the outer wall of the simulated arc.

The exact relationship among the radial distributions of the density gradient, temperature, and the SW is defined through the CEE together with vdW named HMaNF equations in (4)–(14). These relationships could be interpreted in this manner that an abrupt change in the temperature, generates a pressure gradient, which results in a hot fluid, and creates a velocity wave inside it. This wave moves the metal vapor particles, which are heavier than the fluid species. So, the major amount of the generated metal vapor packed together at the CS between the first and the second waves and then, in wave's front. The CS is the result of the sonic barrier when transonic speed travels from subsonic to supersonic ($Ma > 1$). This pack goes out of the arc zone after 1 μs in this case and the mixture density in the simulated distance is reduced from 8900 to less than 2 kg m^{-3} in 8 μs after the explosion. Breakdown in gas mixture happens at 94, 160, and 645 μs, at 1028, 570.4, and 293 V for 25, 40, and 100 μm Cu-EEW at 1 bar N_2.

As was mentioned, the three stages followed by the arc plasma are not separated and overlap with each other. It means at the end of the warming stage, the vaporization makes a two-phase system and affects the boiling temperature of melted wire. When the streamer happens, the shock wave is traveling far from the arc core. For instance, figure 8(b) depicts the pre-burst pressure used in stage I to calculate the wire temperature is about 6000–7000 bar and the wave temperature at the start of EWP shown in figure 6(b) shall be equal to the calculated wire temperature at the start of EWP in stage I (7800 K).

Figure 9 compares the Schlieren-like representations for velocity by the explosion of a 40 μm and a 100 μm thick copper wires exploded at 182 and 530 μs (current source is similar for both cases but the instantaneous current at the time of the explosion is different).

EWP starts at 116, and 529 μs, respectively, and it takes 44 and 116 μs for plasma formations. The general form of plots and so the flow regime is similar. Figure 10 shows time-tagged curves of (a) shock velocity, (b) density, (c) pressure, and (d) ρ-u interactions for the first 1 μs in the explosion of 40 μm Cu wires, at 1 bar N_2 and figure 11 shows *u*, ρ for 100 μm EEW, respectively.

As is shown in figure 10(d), the velocity is increasing from the first instance of the explosion, t_0, to reach the sonic barrier and after a reduction in the wave velocity, the second wave starts to propagate. The speed of the second wave's front is

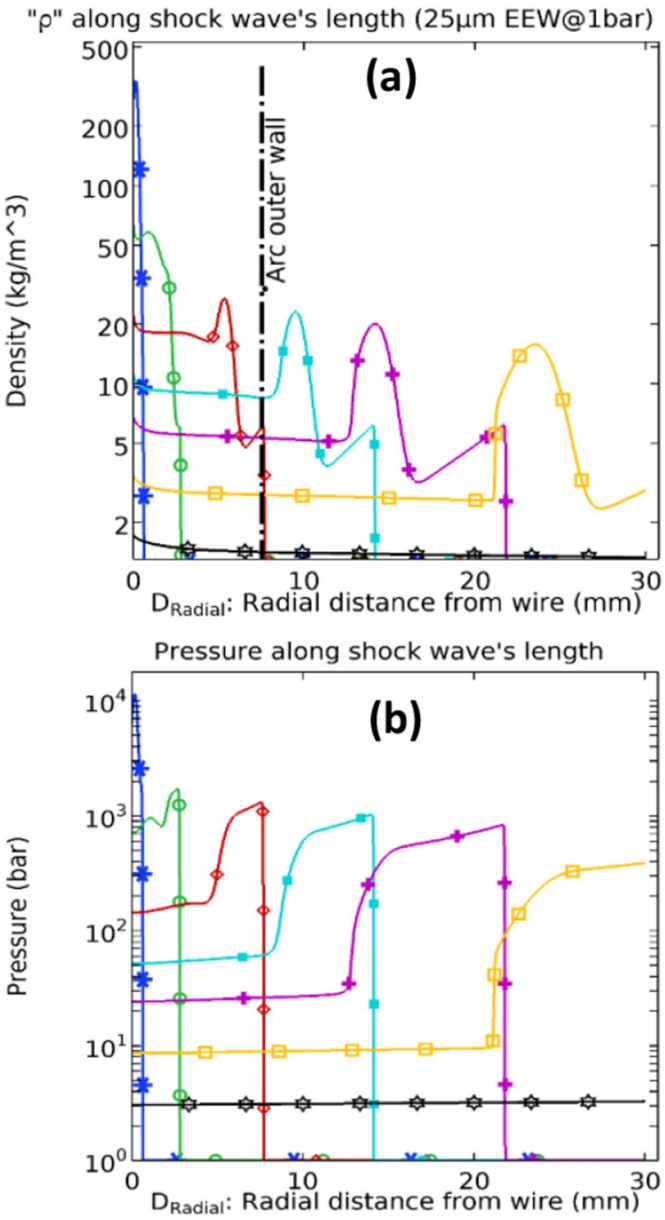

Figure 7. The time-tagged curves of (a) density and (b) pressure distributions in the explosion of 25 μm Cu wire at 1 bar N_2 (the legend and time-taggings are like figure 5).

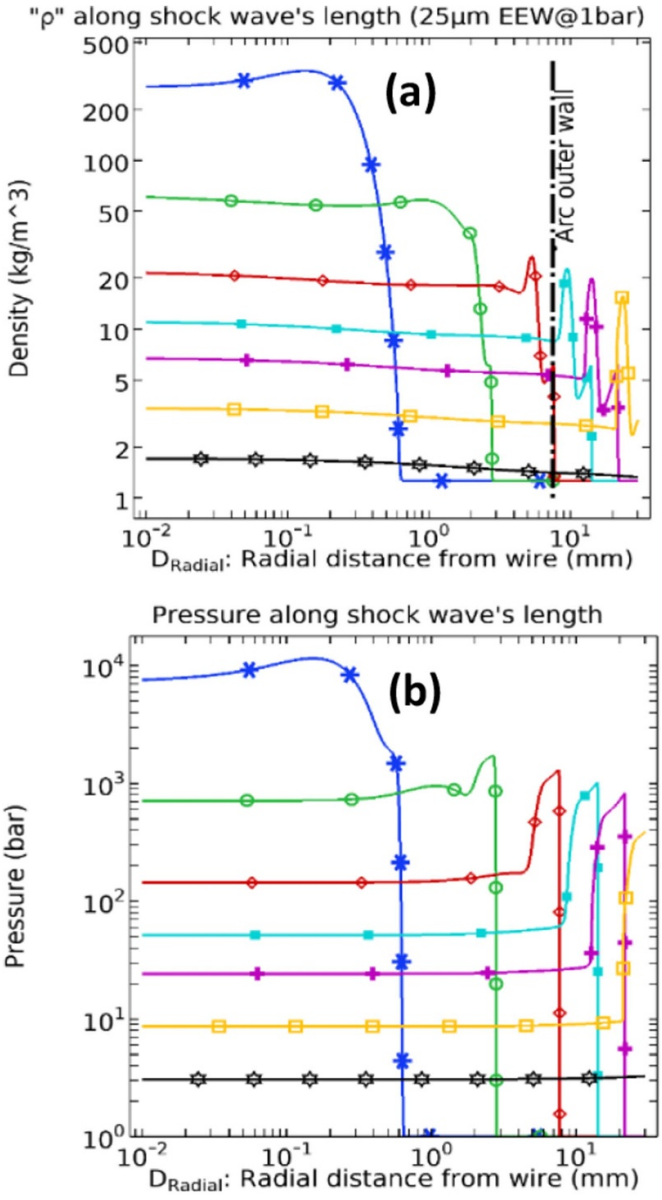

Figure 8. Log-Log view of time-tagged curves of (a) density and (b) pressure distributions of figure 7 (the legend and time-taggings are like figure 5).

decreasing by the time. The density at t_0 is in its maximum and starts to be reduced through spreading by the velocity wave.

The heavy metal particles are accumulating in the wave-front but when the CS is created it works as a trap for metal particles, due to lower velocity at this position compared with the second wave's front. So, the particle accumulation changes to become dominant there. This transition happens for the 40 μm EEW at 350–440 ns, but for 25 μm EEW it occurs at 120–180 ns, while for the 100 μm EEW it is at 8.16 μs (see figure 11(b)) due to different wave velocities.

By increasing the wire diameter while the driving voltage and circuit elements are fixed, the energy density deposited in the wire is reduced according to equation (28). If the gas breakdown due to streamer does not occur until the full energy is deposited in the wire, the expansion rate of copper vapor will be more rapid compared to the case where a small fraction of the energy is deposited before the voltage collapse [36]. Thus, the maximum velocity for a 40 μm thick copper wire (see figure 10(a)) is 7500 m s^{-1}, while it is only 650 m s^{-1} for a 100 μm wire (see figure 11(a)). The comparison for the distribution of the density and pressure waves between the explosion of 40 μm-Cu wire and 100 μm one is raised from figures 10 and 11(b) and (c). The peak of the mixture density passes the arc wall after 1.4 μs and 15–18 μs, respectively. By comparing figures 10(c) with 8(b), it is observed the high pressure is generated within a few millimeters of the wire. The initial SW peak pressure can be increased by slightly reducing the wire diameter (1 GPa in 1 mm from the wire at 40 ns which is

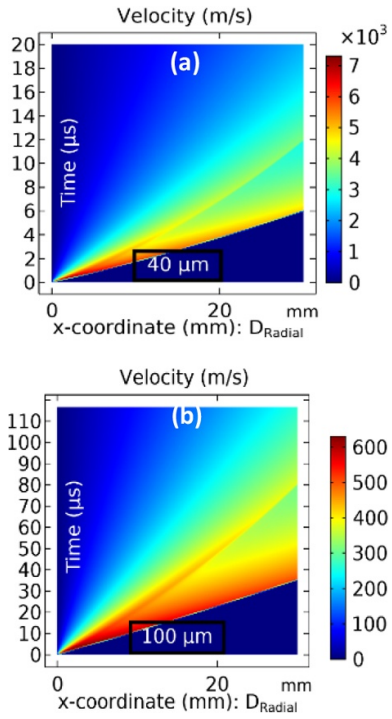

Figure 9. Comparison of Schlieren-like representations of shock velocity in the explosion of (a) 40 μm and (b) 100 μm wire at 1 bar N_2.

reduced to 0.6 GPa in 10 mm at 600 ns and 0.02 GPa in 30 mm at 4 μs in figure 8 (b)).

High-pressure generation further than a few centimeters from the wire requires decreasing the peak pressure attenuation rate by choosing the optimal discharge related to the wire size (0.1 GPa in 4.3 mm from wire at 450 ns in figure 10(c)) or increasing the initial stored energy, otherwise low pressure like what happened in 100 μm EEW will occur. Furthermore, it confirms other research [10].

3.1.2. Effects of filling pressure. In this section, the explosion of 25 μm-Cu wire in nitrogen at the pressures of 20, 40, and 80 bar are studied. The molar ratio of the metal vapor in the mixture is calculated and shown in percentage. Figure 12 shows Schlieren-like representation of the simulation results of Mach number, and mass flow for the explosion of 25 μm-Cu wire at 20–80 bar nitrogen. The *Ma* is reduced from 2.5 to 1.2 by increasing the filling pressure from 1 to 80 bar, while the maximum temperature is almost the same in all cases (see figure 13), which indicates a reduction in wave speed while the maximum mass flow is increased.

Ma Schlieren-like plots show that the position of the CS and velocity distribution and therefore the flow regime compared with 1 bar simulation have changed. The figures have the same color scale for a better resolution. Another consequence is clear from the brightness of Schlieren-like representation of the mass flow and the white contours of the rate of the change in density ($\rho tt = \partial^2\rho/\partial t^2$). The increment in pressure

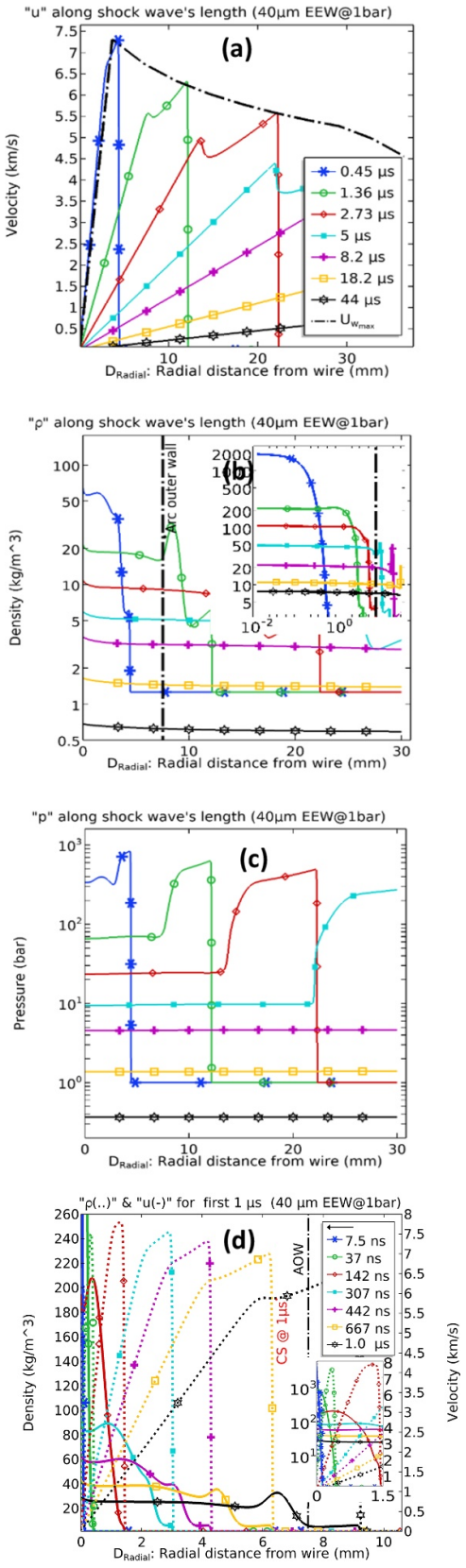

Figure 10. Time-tagged curves of (a) shock velocity and the envelope of front velocity, (b) density, (c) pressure, and (d) ρ-u interactions for the first 1 μs in the explosion of 40 μm Cu wire at 1 bar N_2.

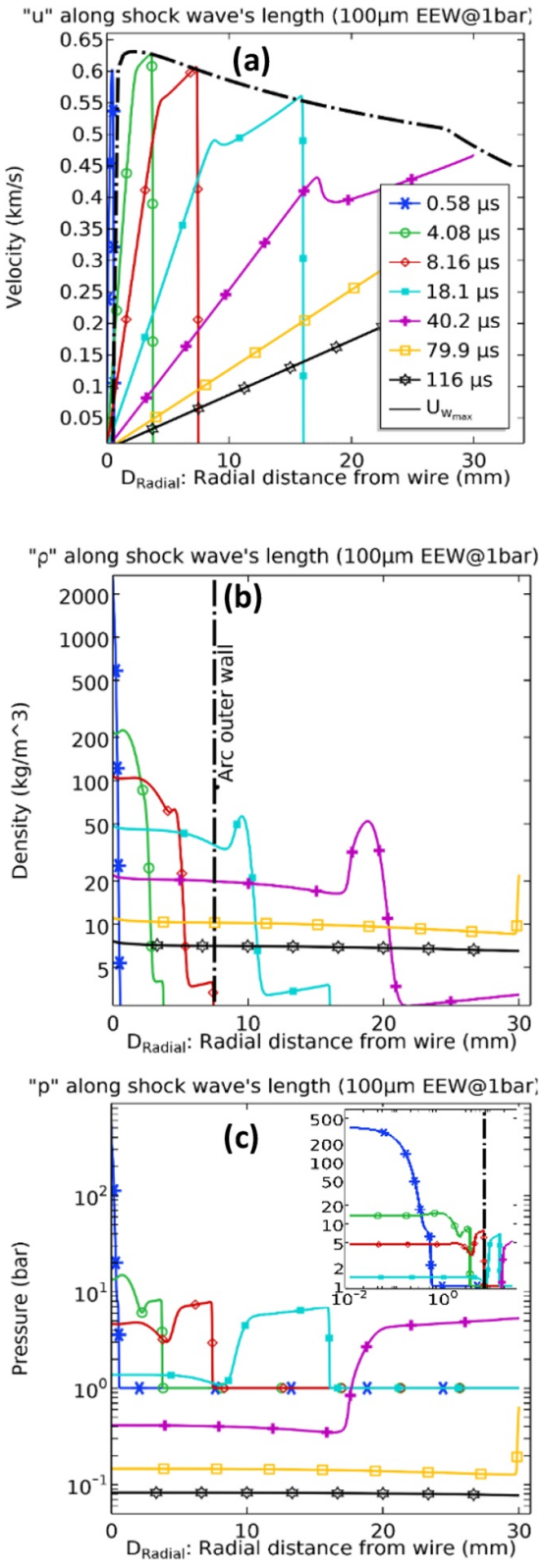

Figure 11. Time-tagged curves of (a) shock velocity and the envelope of front velocity, (b) density and (c) pressure in the explosion of 100 μm Cu wire at 1 bar N_2.

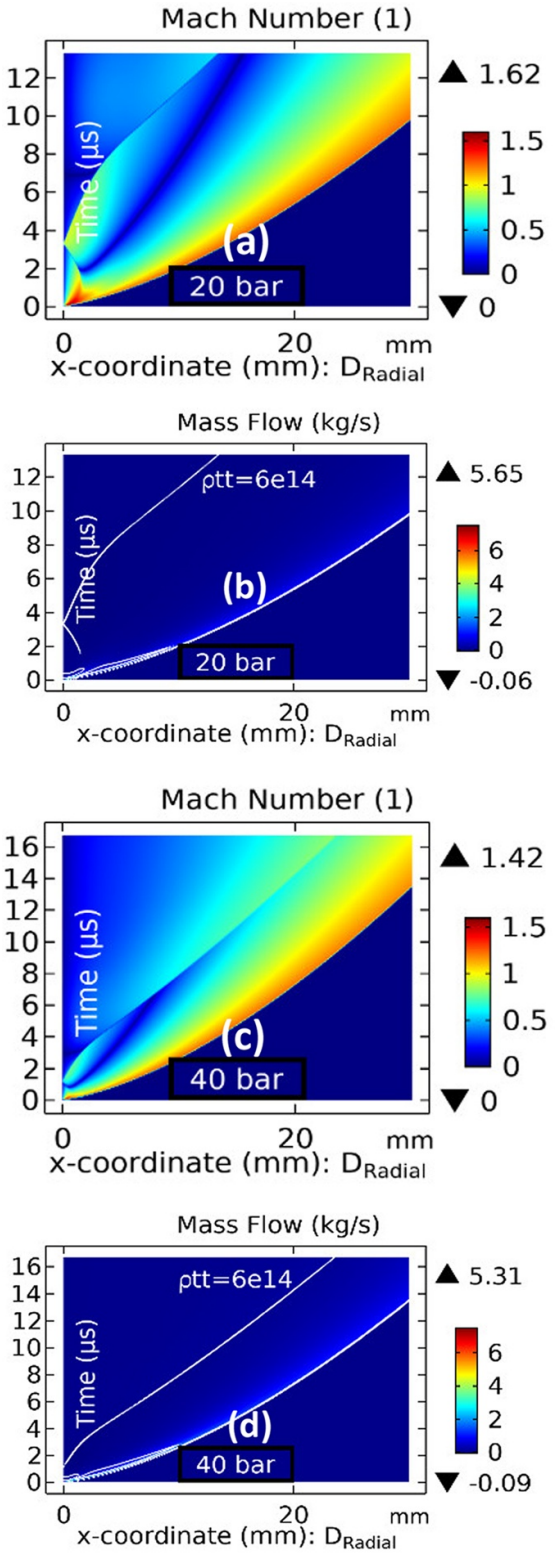

Figure 12. Schlieren-like representation of Mach number, and mass flow and $\partial^2\rho/\partial t^2$contours at 6×10^{14} kg m^{-3}s^{-2} for the explosion of 25 μm copper wire at (a), (b) 20 bar, (c), (d) 40 bar, (e), (f) 80 bar, (g), (h) 100 bar nitrogen with the same scales.

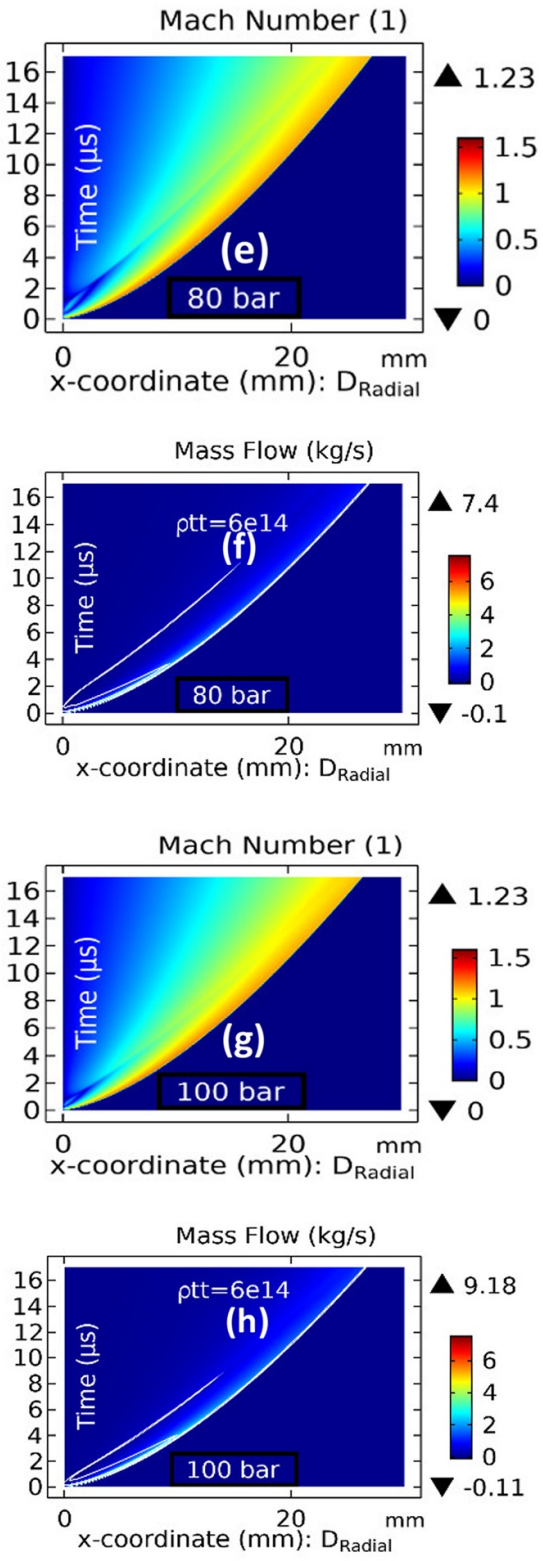

Figure 12. (Continued).

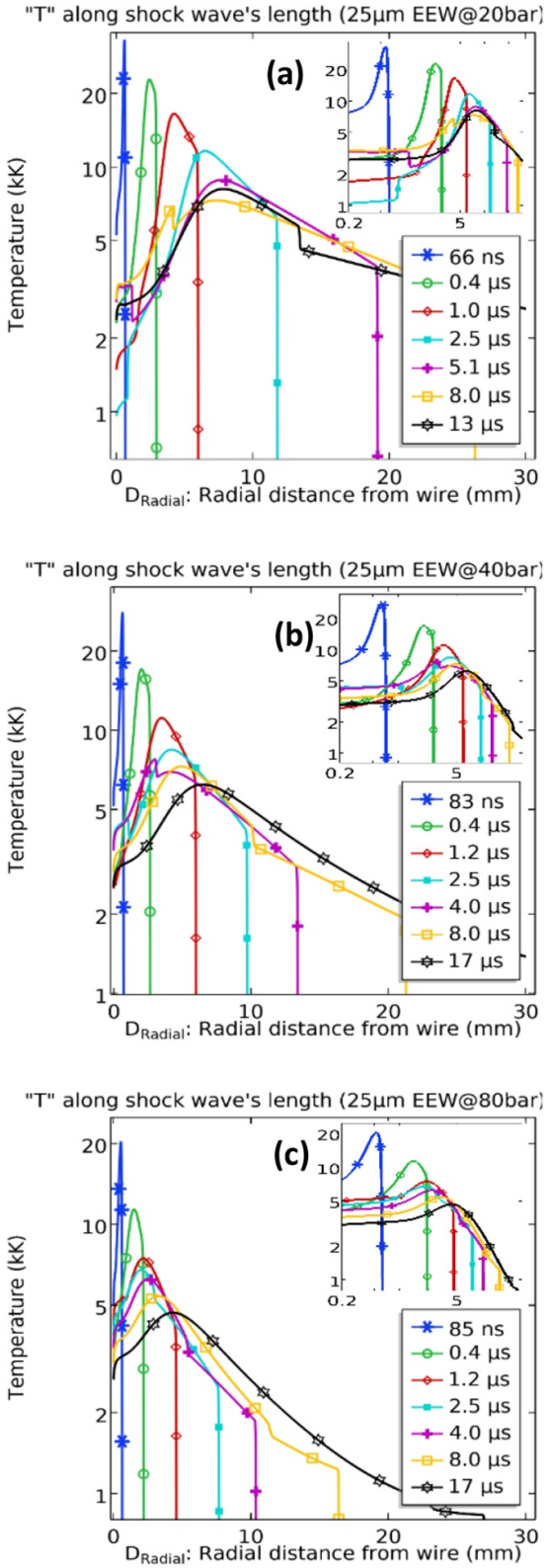

Figure 13. Temperature distribution for the explosion of 25 μm copper wire at (a) 20 bar, (b) 40 bar, and (c) 80 bar nitrogen.

shifts most of the vaporized material from the CS positioned between the first and the second wave to the wave's front and compressed it there. Therefore, it increases the metal percentage in the arcing area. It is validated by calculated molar mass inside the arcing area shown in figure 15.

As ρtt contours at 6×10^{14} kg m^{-3}s^{-2} shows, 20 bar case behaves differently from other cases here and even from 1 bar case. This difference has a practical consequence, which is

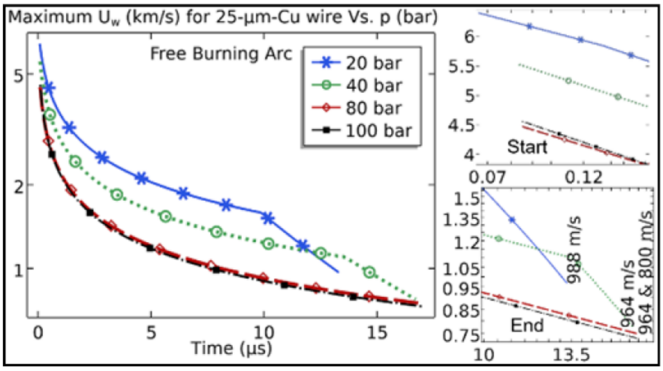

Figure 14. Maximum front velocity for the explosion of 25 μm copper wire in 20–100 bar nitrogen.

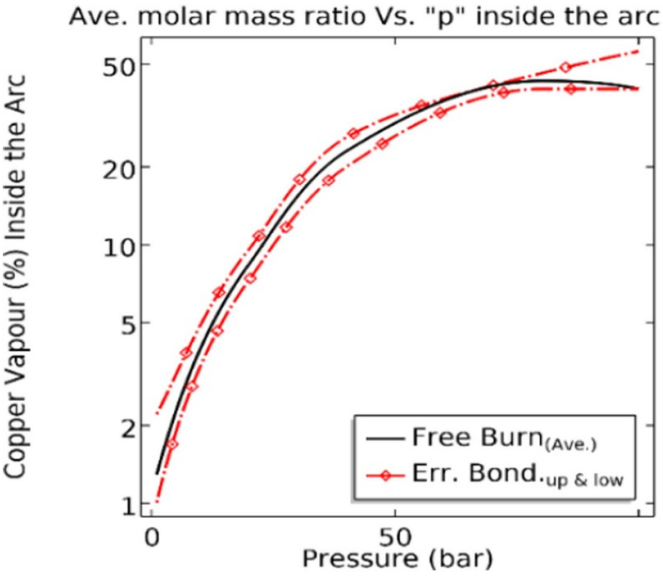

Figure 15. $X_{mixture}$% inside the FB arcs at the time of PF for the explosion of 25 μm Cu wire at 1–100 bar N_2.

shown in figures 16(c) and (d) and will be explained in the discussion.

The change in flow regime and higher thc_{tot} of dense gas make the temperature distribution in figure 13 smoother compared with figure 6. Increasing the filling pressure results in higher maximum mass flow (here the maximum mass flow is increased from 5.65 kg s^{-1} at 20 bar to 7.4 and 8.19 kg s^{-1} at 80 and 100 bar, respectively), in higher thc_{tot}, in higher withstand level and in higher mass densities. However, a higher filling pressure will reduce the wave velocity. Filling pressure increment will increase wave attenuation rate, too. In these cases, from 7500 m s^{-1} to 5000 m s^{-1} in 90 μs for 1 bar as shown in the envelope of figure 10(a) versus from 4500 m s^{-1} to 800 m s^{-1} in 18 μs for 80 bar nitrogen in figure 14.

Consequently, the total mass flow is reduced by increasing the pressure to some extent. The simulation shows that a pressure increment from 80 bar to 100 bar is almost ineffective on the wave speed, although it increases the maximum mass flow to 9 kg s^{-1} (see figure 12(h)), which results in total mass flow increment and therefore, in lower metal content percent than 80 bar (see figure 15). The moment where the voltage peak changes its slope due to the breakdown is associated with the PF and from this instant on the metal vapor in the arc area in non-blasting cases is almost unchanged due to the wall created by the difference between densities inside and outside the arc next to it [6]. Thus, this time will be used to calculate the average of the $X_{mixture}$% inside the arc area shown in figure 15 as the arc metal content up to 100 bar.

3.1.3. Effects of the cylindrical nozzle. Inserting cylindrical nozzles between electrodes affects the flow equations by changing the boundary conditions in the study. The length and the inner diameter of the nozzle as well as its position between the electrodes are varied parameters in this study.

As shown in figure 1, two-centimeter-long cylindrical nozzles with internal diameters of 4 mm and 2 mm (OpOp _4 and 2 in figures 16(c) and (d)) are added in the middle of the electrodes and the 25 μm-Cu wire explosion in nitrogen at the pressures of 20, 40, 80 and 100 bar are simulated. Four more geometries (shown in figure 16(a)) are studied to consider the effects of the nozzle's length and position on the molar ratio of the mixture.

As shown in figure 16(a), W*(i)*O*(j)*_*(k)* comes for *(i)* mm long nozzle with *(k)* mm diameter when one end is walled and the other end is open, and the open end has *(j)* mm distance from the electrode. The symmetry in all dimensions results in the reduction of the 3D model to 2D ones. The physics of nozzle is strongly symmetric and can be assumed 2D, with the physical properties having gradients both in the y-direction (axial) and x-direction (radial). However, a full 2D model would be expensive in processing time. Another simplification is applied to decouple the 2D model into two separate 1D models in the 'x' and 'y' directions without losing accuracy based on the superposition rule. When the explosion starts, SW starts to expand freely before reaching the closed wall of the nozzle in the middle of its radial expansion route.

According to figure 16(a), the explosion generates waves W_{x1} outside and W_{x2} inside the nozzle. When W_{x2} reaches the walls, it is reflected on its tail and then is relieved from open ends of the tube in 'y-direction' perpendicular to the free waves generated in sections between nozzle and electrodes and generates another SW in the y-direction named W_y. The waves' travel time in x-direction inside the tube is shown in figure 16(b) and varies from 720 ns to 2 μs depending on the pressure and the nozzle diameter. Another simulation in the y-direction with the initial condition obtained from the first simulation at t_{travel} starts. The wave W_y starts when W_{x1} has moved away to $d_{travelled}$, whereas the metal vapor of the free end(s) has moved far away from the wire position (centerline) and the superpositioning rule will be applied on both densities obtained from x and y directed shocks to calculate the density of the mixture in the arcing area outside the nozzle. The metal vapor in the mixture is shown in percent in figures 16(c) and (d) for all six cases studied up to 100 bar. Figure 16(c) illustrates the consequence of different mass flow behavior at 20 bar in figure 12(b) that is repeated here for the one-end closed nozzle. This behavior results in a high level of metal vapor inside the

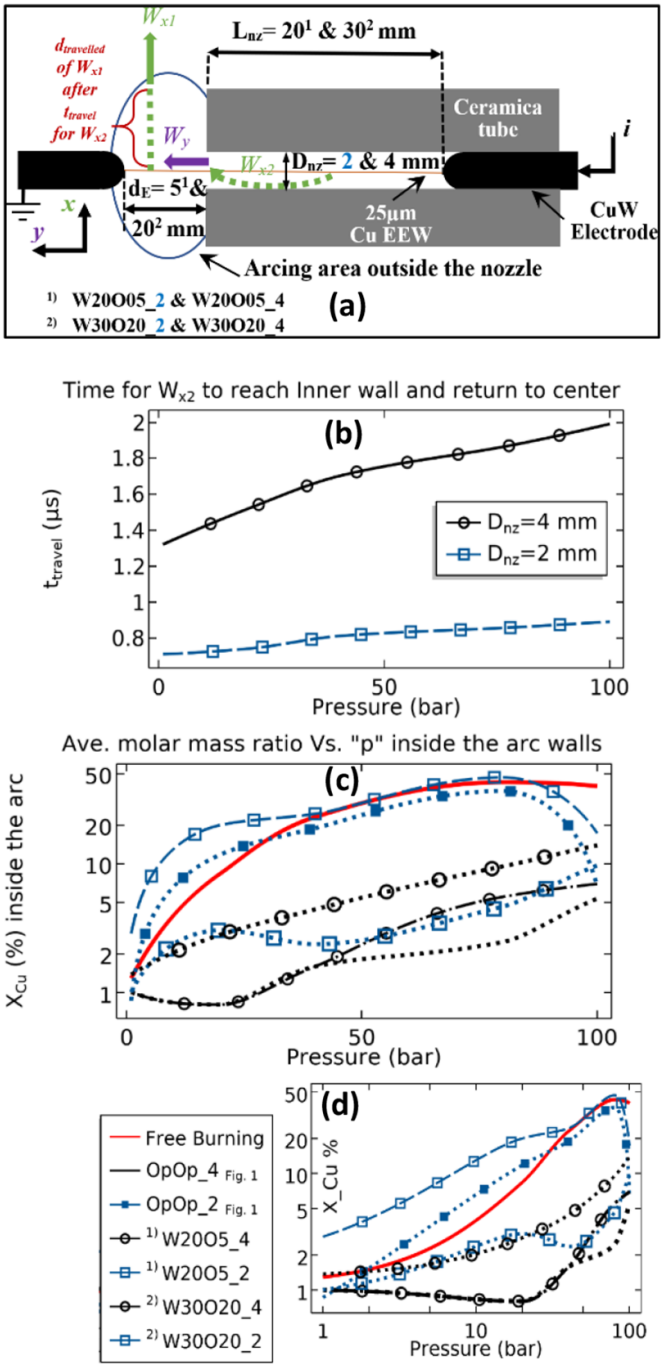

Figure 16. (a) Schematic of the one-end closed nozzle, (b) travel time for SW to reach the inner walls of 2 and 4 mm-diameter nozzles and return, (c), (d) X_{Cu}% inside the arcing area, for nozzle constricted arcs at the time of PF; 25 μm-Cu EEW at 1–100 bar N_2.

arc for the 20 bar cases that is almost equal to 70–80 bar case studies. Figure 16(d) shows for the pressures lower than 6–7 bar for cases with both side open nozzle named open-open (OpOp), the amount of metal vapor is less than 2.4%. Thus, utilizing the EEW does not affect the CB model so much and remains still a practical method for the study of the CBs in ordinary pressure levels while it will not be a proper choice in the study of CBs utilizing SCF as insulating gas (SCFCB).

Wave W_{x2} is shown in the velocity plots of figure 17 for the different pressures and nozzle diameters. The figures have the same color scale and two vertical white lines shown in figure 17(a) are 70 000 K, and 140 000 K temperature contours. Arrows show the mass flow direction and horizontal solid black lines show the area with the reverse mass flow. The solid white contour shows the border between these two mass flows where $\partial\rho/\partial t = 10^6$ kg m^{-3}s. The grey parts are the areas with zero mass flow. The simulation shows OpOp geometries get almost empty of metal vapor at the time of gas breakdown.

4. Ablation

According to figure 17(a), the temperature reaches 140 000 K and even higher in the vicinity of the inner wall of the cylinder in 100 μs. So, the vaporization or the ablation of the polymer material might happen. The details of polymer decomposition are too complicated for describing with a single distribution function as an ablation model, but a widely used simplified ablation equation for the nozzle can also be applied [37] which is considered through (33). If ablation is not too strong and the Mach number is much smaller than one, then $(Ma)^2$ can be neglected. Here, in the stage II : $1.1 \leq Ma_{max} \leq 2.18$

$$\dot{m} = \frac{\delta(T - T_{ablate}) \cdot (T_{ablate} - T)}{(h_v + dh_{PTFE} + 1/2.(Ma)^2)}. \tag{30}$$

The vaporization enthalpy h_v that is necessary to produce gaseous C_2F_4 at 1000 K is set to 2.6 MJkg^{-1} [38]. Besides, the specific heat dh_{PTFE} is taken into account to heat up the PTFE to the effective ablation temperature of 3500 K [37]. δ is again the Dirac delta function. Moving mesh is coupled to calculate the sublimated material in this physics. Details are explained in [6]. The FEM model was verified through the experimental results already published in [39]. The experimental results show at 1 bar, a total nozzle mass loss of 9.2 mg was measured after five tests on 50 mm long nozzle with 4 mm diameter. The error of the weighting tool was ±0.5 mg. Figure 18(a) shows the ablated mass for the arc current of 135 A and 190 Hz for $D_{nz} = 2$ and 4 mm with an average ablation rate of 25–30 mg kJ^{-1}, which is in line with the measured results. Figure 18(b) shows although the gas temperature in the vicinity of the inner wall is very high but the wall temperature for $D_{nz} = 2$ mm, cannot reach temperatures higher than 1000 K in the first microsecond and therefore, ablation starts from 1300 μs. When the arc current falls below 60–70 A the nozzle temperature falls below 2400 K and the ablation stops until the second half cycle which again continues with higher rate due to higher temperature as a result of pre-warming from previous half cycle (see figure 18(b)). It should be noted that $Ma \leq 0.3$ after the PF.

5. Streamer breakdown (Schumann criterion), stage III

In section 2.1, it was explained that the current is carried by the melted wire before it is dispersed in nitrogen by the SW. The

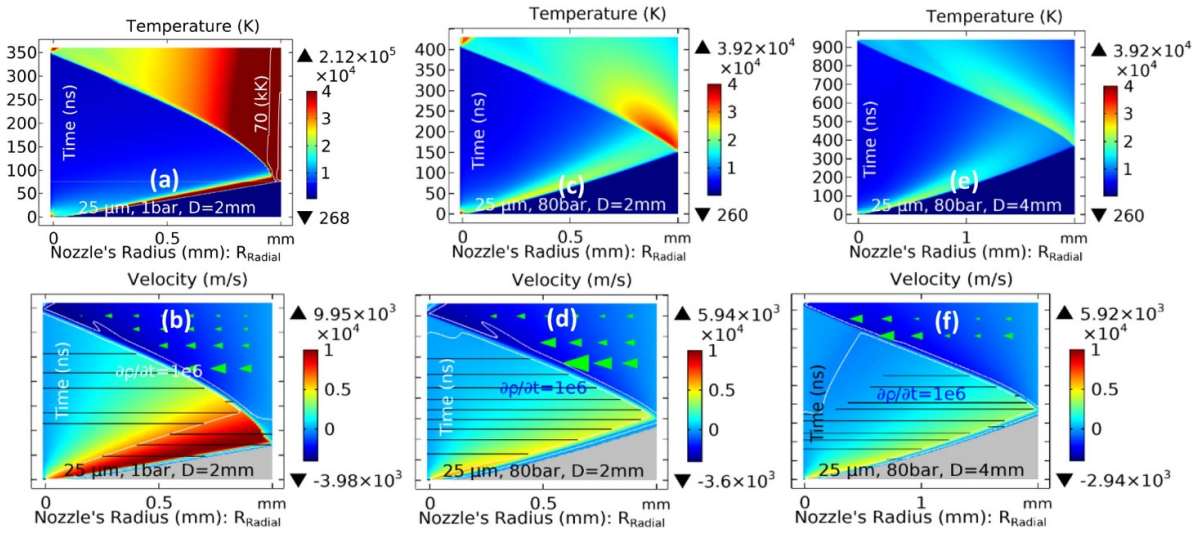

Figure 17. Schlieren-like representation of temperature and velocity for W_{x2} in (a), (b) 1 bar for $D_{nz} = 2$ mm, (c), (d) 80 bar for $D_{nz} = 2$ mm, (e), (f) 80 bar for $D_{nz} = 4$ mm in the explosion of 25 μm Cu wire inside N_2.

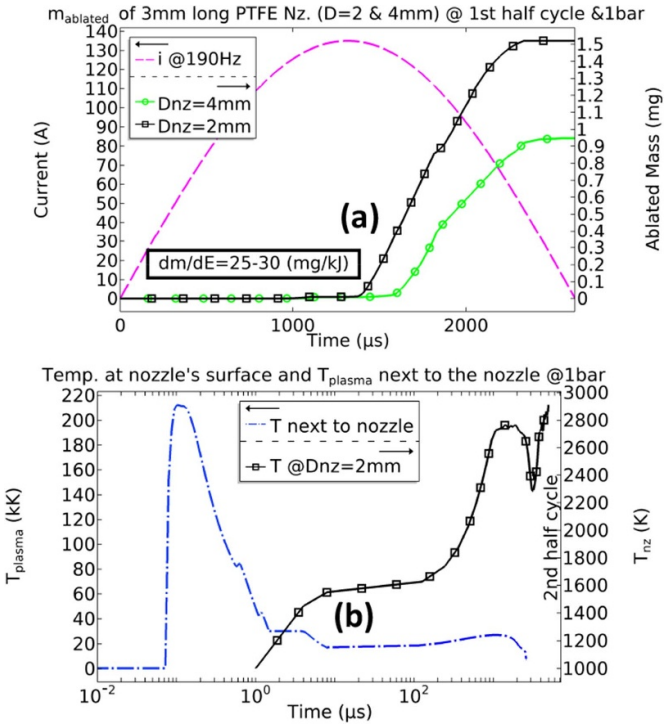

Figure 18. (a) The ablated mass of PTFE in the first half cycle for 190 Hz-135 A arc current and $D_{nz} = 2$ and 4 mm, and (b) gas temperature in the vicinity of the inner wall and wall temperature for $D_{nz} = 2$ mm, in the explosion of 25 μm Cu wire inside 3 cm long PTFE nozzle at 1 bar N_2.

reduction of the conducting part of the melted wire by vaporization results in a sharp increment in the wire resistance and consequently in the voltage drop across the wire (see figure 2(a)). This voltage increment is limited by the breakdown of the surrounding gas mixture. At high values of pressure multiplied by electrode distance (p.d), including in high-pressure non-uniform configuration, the breakdown in gas is mostly of a streamer type. These streamers can result in the partial or complete breakdown of the gaseous insulation in non-uniform field gaps depending upon the field configuration, the type, and pressure of the gas, the mixture ratio, and the waveform of the applied voltage. Here the static voltage is applied. The Schumann streamer inception criterion is:

$$\int_0^d (\alpha - \eta) \cdot dx = K = Ln(N_{ec}), \tag{31}$$

where α and η are the ionization and the attachment coefficients, respectively, which both depend upon the electric field intensity and the gas number density or pressure in the gap. The integral boundary is d, which is the length of electric field lines between the electrodes. The critical avalanche size is K, which is for N_2 considerably smaller than the generally accepted value of 18.42 (for the critical number of electrons, $N_{ec} = 10^8$) and shall be estimated based on experimental results in each interval of a reduced electric field [40, 41]. The general form for K suggested in [40] is:

$$K = 5.75 - 0.76 \ln(pd)\,; 5x10^{-2} < pd < 10\,\text{bar} \cdot \text{cm}. \tag{32}$$

The electrical breakdown voltage is calculated by integrating Townsend growth coefficients (TdGC) of the mixture along the electric field lines. Figure 1 shows the 3D geometry used for the simulation of streamer breakdown based on the Schumann criterion for the explosion of 25 μm copper wire inside the nozzle with both ends open (vaporized wire was dispersed inside the vessel).

Figure 19 shows simulation results for a gap length of 0.03 cm using equation (32) and the experimental breakdown voltage for pure N_2 at different pressures [42]. Compared with simulations, the fitted curve to experimental results shows increasing deviation from the similarity law at high gas pressures and high electric fields, $E_{br} > 10^5$ V cm^{-1}. The distance between the electrodes is 3 cm in our study, so according to equation (29) using K is valid just for 1 bar tests and for higher

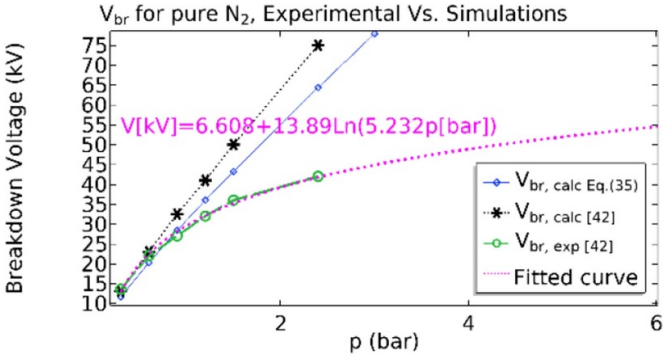

Figure 19. The experimental breakdown voltage for pure N_2 at different pressures versus simulation results.

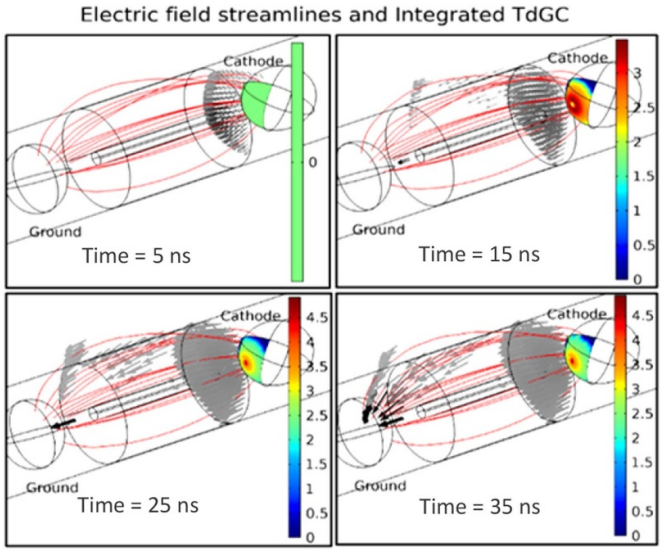

Figure 20. Integrated TdGC, avalanche, and streamer breakdown for the explosion of 25 μm Cu wire inside the nozzle at 1 bar N_2.

pressures or equivalently higher distances, another model considering 8–11 reactions including the excitations, ionizations and attachments shall be solved numerically [43]. Technical grade (TG) N_2 which can have up to 1% oxygen [44] was used in experiments and considered in simulations due to its small effects on the attachment coefficients.

BOLSIG+ [45] with LAPLACE database [46] is used to calculate the TdGC at different mixture ratios of nitrogen/-copper vapor obtained from OpOp_2 and OpOp_4 curves in figures 16(c) and (d). Figure 20 shows the unitless indicator of integrated TdGC, electron avalanche, and streamer breakdown for the explosion of 25 μm Cu wire inside the nozzle at 1 bar nitrogen. The arrows are proportional to the avalanche electron number density. Integrated TdGC across the nozzle tunnel is shown as a colored surface on the cathode. Although the nozzle increases the electric field between the electrodes, it also works as a barrier for most of the electrons. Still, the electron density on the shortest route which arrives faster to the other electrode through the nozzle makes the streamer.

It is observed that discharges start at lower voltages than expected due to ultraviolet (UV) radiation and the exploding shocks which may have ionized the nitrogen [47]. The average external field that was necessary to sustain the steady growth of a streamer in N_2, E_s in the experiment, is almost independent of gap length and field inhomogeneity. In TG-N_2, $E_s = 1.5$ kV cm^{-1} at 1 atm is considered. The value of E_s is very sensitive to the attachment. If N_2 is heated to 1000 K, electrons are liberated from negative ions and E_s falls to 0.4 kV cm^{-1}. The necessary field also increases as the humidity is raised [44].

6. Discussion

6.1. The arc metal content for different wire sizes

The calculations are compared with experiments using 25, 40, and 100 μm copper wires surrounded by 1 bar N_2 (see details in [27]). Figure 21 depicts the measured values of *V, P* (voltage multiplied by current), and *R* (voltage divided by current) for 20 μm EEW with a sampling rate of 1.25 Msamples per second, 40 μm and 100 μm EEW with a sampling rate of 500 Msamples per second in the logarithmic scale. In contrast to the well-known pulse with dwell (current pause), a single electrical pulse is produced [48], which is usual for relatively low resistive metals like copper [49] although it is also possible to have a current pause with 25 μm EEW, (for instance see figure 4 in [50]). The heating process changes to an explosion after 76, 116, and 529 μs from the current injection corresponding to 25, 40, and 100 μm, respectively, which results in the change of the voltage slope. Here, the PF occurs 8, 44, and 116 μs after the explosion, t_0. These three intervals were simulated in section 3.1.1.

It is explained in [26] through synchronous imaging and assuming a constant wave speed, small changes in T and at the absence of restriking, that the time of melting completion and explosion as well as the time of the voltage maximum can be estimated with low accuracy through the small oscillation in the I (see figure 21(b)). The average wave velocity, $\bar{U}_w$, is estimated from wire radius, r_{wire}, delay between the peaks of V and P, Δt, and the peak of the R, R_{peak}, which are extracted from figure 21, and L_{cir}, according to (33) [1]:

$$\bar{U}_w = r_{wire} \cdot R_{peak}/(2 \cdot \Delta t \cdot L_{cir}). \tag{33}$$

The R_{peak} and Δt are 54.1 Ω/1.7 μs, 11.48 Ω/1 μs, and 2.02 Ω/3.75 μs, for 25, 40 and 100 μm thick Cu wires, respectively. This resistance anomaly was already reported for a tiny gold wire in the air [26] and underwater aluminum wire [51] through the circuit parameter tuning but we report on the first observation of the interaction between the nozzle, the pressure and the metal content of arcs. The expansion velocities at t_0 and at the time of the PF, i.e. when the voltage peak changes its slope are numerically simulated at about 11 000/3746 m s^{-1}, 7300/2900 m s^{-1}, and 630/360 m s^{-1} (see figures 5, 10(a) and 11(a)) while the average velocity is estimated as 4630 m s^{-1}, 2670 m s^{-1}, and 313 m s^{-1} through (36). Figures 22(a) and (b) show NEC and electrical conductivity (σ) while figures 22(c) and (d) show heat capacity (c_p) and thc_{tot} for N_2 and N_2-Cu

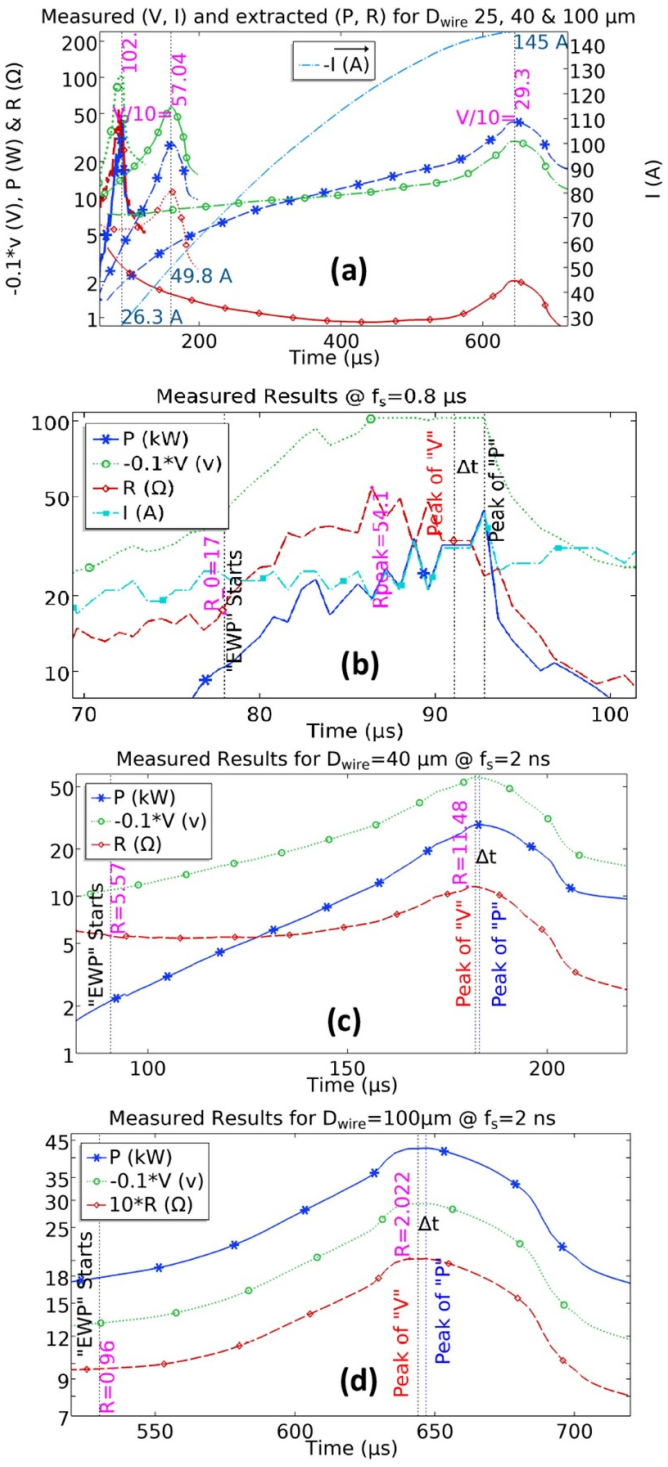

Figure 21. Voltage, power, resistance, current for (a) 25, 40 and 100 μm, (b) 25 μm, (c) 40 μm, and (d) 100 μm Cu EEW at 1 bar N_2 in FB.

vapor mixture with different mixing ratios up to 25 000 K at 1 and 80 bar, all calculated in PLASIMO. NEC is calculated for the sphere radius $R_p = 0.5$ mm at 1 bar and 0.05 mm at 80 bar, which can be considered as an average radius of the hottest regions. NEC is almost independent of pressure while the σ is highly dependent. From the Dumas method in equation (29), the calculated amount of copper inside the arc at the time of PF, i.e. 84, 182, and 530 μs after current injection are 1.29%, 2.83%, and 2.24%, respectively, for 25, 40, and 100 μm Cu EEW. As is clear from figure 22, these small amounts of metal vapor have a considerable influence on σ and the NEC but a negligible effect on the c_p and especially thc_{tot} at 1 bar [52]. From figure 22(b), adding 0.43% Cu increases σ from 1 to 100 S m^{-1} at 5 000 K at 1 bar while adding more copper vapor up to 3.27% just changes σ to 150 S m^{-1}. But adding 18%–41% copper vapor to N_2 at 80 bar and 5 000 K increases the σ from 0.1 to 20 S m^{-1}. Despite the difference in the wire diameters, the metal content at the time of PF is almost equal in three case studies that result in similar σ and NEC much different from pure cases and this could explain the arc voltage equalities despite few differences in metal vapor content. Another crucial parameter for the MHD simulation is viscosity (η). As shown in figure 22(e), η is more sensitive to pressure than to the metal vapor content. These transport properties in addition to ρ for the exact mixture ratio from this study are calculated through PLASIMO code and used in MHD tools in a recursive method that resulted in an accurate voltage simulation [6, 35], which points in the direction that the calculated mixture ratio is realistic. The arrows in figure 21 show that, as the filling pressure is increased, the extremums of c_p and thc_{tot} are reduced while the peak of η is increased, and all shift towards the high temperature. The arc temperature just near current zero (CZ) is less than 4 000 K. The thermal interruption capability of a gas is dependent on ρCp as a factor. the ρCp_{peak} produces a corresponding peak in turbulent thermal conductivity, which results in a broad radial T-profile and a large arc radius [53]. For optimum thermal interruption performance, the ρCp should be as large as possible at temperatures below the '$T_{conducting}$' (around 4000–5000 K) and as small as possible at higher temperatures [54]. Figure 22(f) shows that ρCp in 40 bar for 4000 K $\leq T \leq$ 4500 K, is equal to the ρCp for 80 bar while its η is smaller. The legend for the 1–40 bar in figure 22(f) is like figures 22(d) and (e).

6.2. Experimental appraisal of SW expansion time, t_0

The energy density, ε, for 25 μm case was 2.09 J mg^{-1} while it was 1.18 J mg^{-1} and 0.0074 mJ mg^{-1} for 40 and 100 μm EEW, which meets the slow explosion criteria [2]. Figure 23 depicts the measured voltages between 75 and 82 μs for 25 μm copper EEW explosion at 1, 20, and 80 bar filling pressures. It shows the start of EWP at 76–77 μs which is in line with simulated results of figure 3. It shows that the start of EWP, t_0, is independent of pressure and nozzle effect but depends on the wire diameter and ε, the energy density of the wire. It also confirms that conduction and convection are negligible for the heating model, as all voltages before the start of expansion have the same value during the heating stage at different filling pressures and therefore different conduction and convection.

6.3. Interruption performance; nozzle-pressure effects

As is shown in figure 16(c) at pressures between 20 and 80 bar, the copper content of the arc initiated by the ignition wire, is

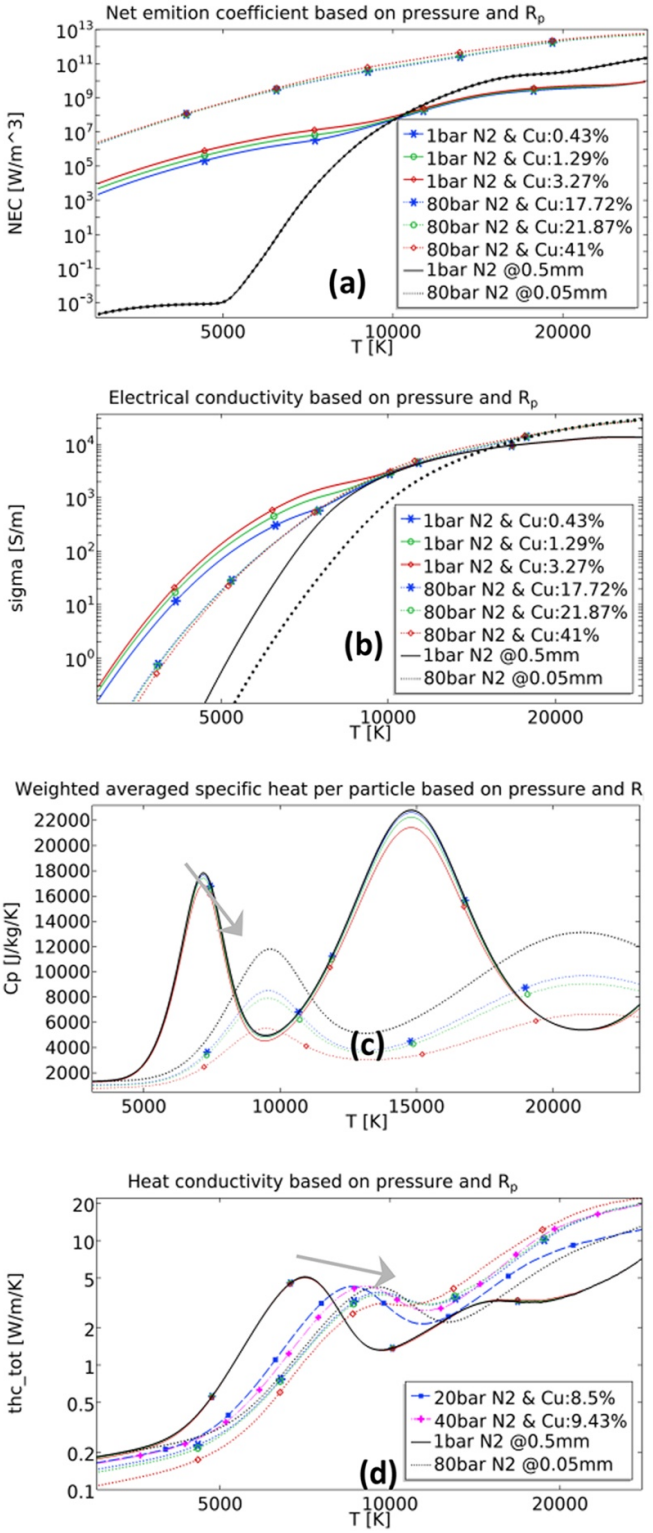

Figure 22. (a) NEC, (b) electrical conductivity, (c) heat capacity, (d) total heat conductivity of N_2 and N_2-Cu at 1 and 80 bar, (e) viscosity, and (f) $\rho.c_p$ of N_2-Cu at 1, 20, 40 and 80 bar.

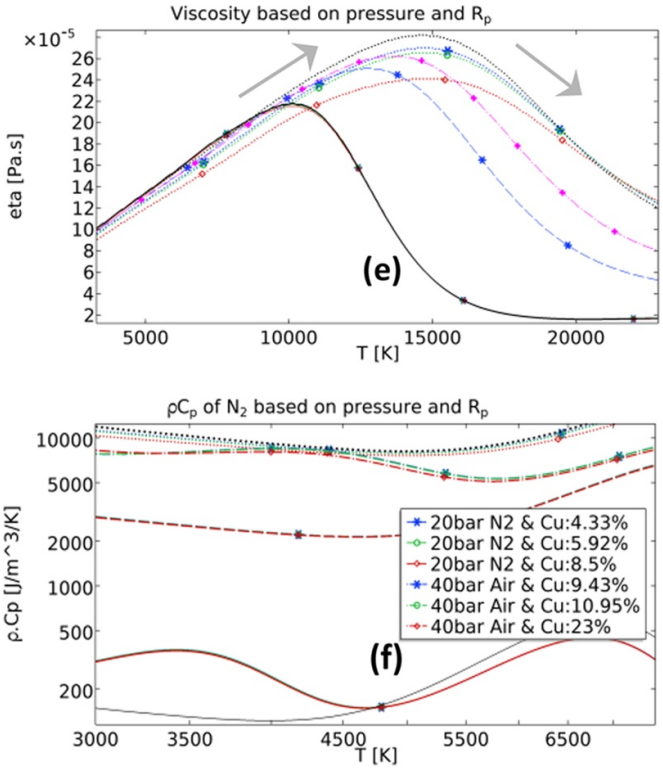

Figure 22. (continued).

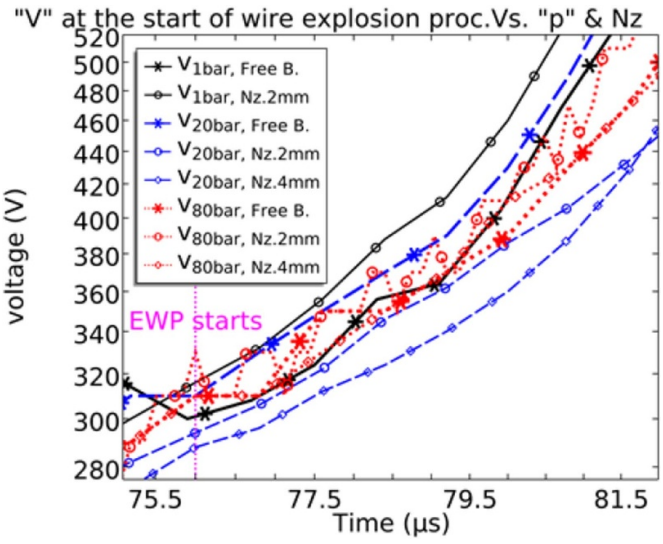

Figure 23. Measured voltages between 75 and 82 μs for 25 μm Cu EEW.

between 2% and 45%, and the effect of nozzles on the mixture ratio is not negligible. So, the commonly used method of utilizing EEW in the model CBs instead of contact separation does not apply to SCFCB and complex actuator design, complicated simulation, and measuring methods [22, 55] due to the arc elongation in a dense medium [56] is required for an accurate study.

For instance, the current interruption performance at 20 bar for the tube constricted arrangements with 4 mm inner diameter, is observed to be worse than that at 1 bar, whereas 40 bar shows the best performance in the proposed N_2 CB model [50]. Compared with FB arcs, at higher pressures (5–30 bar), 3 cm nozzle length with 2 mm inner diameter in

both wall-open (W30O20_2) and open-open (OpOp_2) cases result in higher metal vapor. The 2 cm and 3 cm nozzle with 4 mm diameter in wall-open (W20O5_4 and W30O20_4) and open-open (OpOP_4) arrangements all result in a lower metal vapor content. The pressure at which these extremums happen can shift with a change in the nozzle's geometry. For W20O5_4 the metal vapor has a local maximum at 20 bar and a local minimum at 40 bar. As it is shown in figures 22(d)–(f), thc_{tot} increases with p after 13 000 K, while decreases for temperatures less than 8 000 K in both 20 and 40 bar cases. So, cooling is almost the same for these two cases while the metal content of 20 bar case is higher than 40 bar case for W20O5_4 which besides the mass flow (see figure 12(b)). This observation and ρCp for 4000 K $\leq T \leq$ 4500 K in addition to the expansion speed, which is discussed here, can explain interruption failure at 20 bar and good performance at 40 bar.

Another effect of a narrower nozzle from figures 17(b), (d), and (f) is increasing T and changing its distribution inside the nozzle. Figure 24(a) shows the measured voltages for 25 μm copper EEW at 1–80 bar N_2 in FB and inside the nozzle. The legend is the same as figure 24(b).

The advantages/disadvantages of using nozzle tubes for the arc ignited by the EEW are clear from figure 16(c). Besides the arc constricting effect and guiding the cooling flow during the current interruption, it results in evacuating or stocking the metal vapor according to simulations, which are confirmed here with measured values. The arc ignition in a real circuit breaker is because of contact separation which results in ablated materials from contacts and the nozzle. The effects of the nozzle on the distribution of these materials were already studied through the ablation model and particle tracing in [6].

By comparing the voltages at 80 bar pressure for nozzles with 2 mm and 4 mm diameters with these voltages at 20 bar pressure for the same nozzle sizes before the breakdown (figure 23) and after that (figure 24(a)), the measured voltages before the breakdown from figure 23 shows $V_{80bar,\ Nz.2mm}$ is higher than $V_{80bar,\ Nz.4mm}$ but $V_{20bar,\ Nz.2mm}$ is lower than $V_{20bar,\ Nz.4mm}$. After the explosion, from figure 24(a), the voltage in the narrower nozzle at 80 bar pressure is lower due to a higher metal content as it was explained in figure 16(c). From figure 12(b) the mass flow of the metal vapor even for FB arc cases is different from other studies' pressures. Although the temperature-dependent thc_{tot} of the nitrogen at arc temperature near CZ (lower than 4000 K) decreases with increasing filling pressure, it is seen from figure 24(b) that the expansion speed is reduced at 20 bar while it is increased at higher pressures and it will be maximum at 40 bar for 4 mm inner diameter of the nozzle.

These three parameters of metal content, mass flow, and the expansion speed at 20 and 40 bar may explain that the reason for the failure in our tests with 20 bar is a high amount of metal vapor while the metal content of nozzle constricted cases is minimum at 40 bar. Although CZ happens almost after 2 ms, it should be noted that the gas flow inside the arc is as slow as 3.6–40 m s^{-1} after the PF and mostly in the reverse direction towards the arc. Moreover, the arc has a wall due to the difference between inner and outer pressure, and therefore

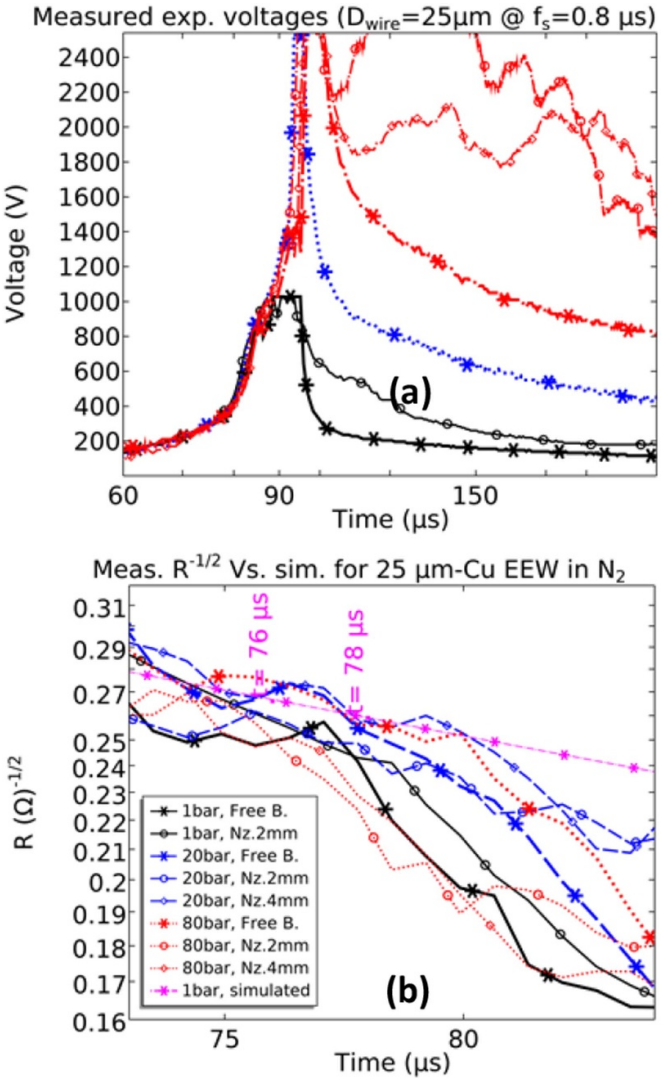

Figure 24. (a) Measured voltages, and (b) measured $R^{-1/2}$ at 1–80 bar in FB and inside the nozzle explosion for 25 μm copper EEW.

it can be concluded that the metal content in the arc remains rather high [6].

7. Conclusion

During the explosion of copper wires at a temperature range of tens of kiloKelvin radiation, the vaporization temperature is considerably higher than the boiling as the vaporization occurs in saturated vapor pressure.

The expansion wave speed has a crucial role in dispersing the metal vapor of EEW and it is related to energy density injected into the wire. Observations from conducting experiments have shown that the arcing voltage a few hundred microseconds after the explosion of the different wire diameters (25, 40, and 100 μm) is almost equal. In contrast, the initial voltage peak delays and magnitudes during the EWP are different due to differences in wire's energy density, and therefore, the wave speeds.

The time of explosion for EEW of similar diameters, in contrast to the expansion wave speed, is independent of filling pressure or presence/size of the nozzle, and just depends on energy density. Therefore, the initial voltage peak delays are similar while the magnitudes during the EWP are different.

The choice of wire and power supply parameters should be based on the radial position where high pressure is required in utilizing EEW for other usages than circuit breakers.

Although increasing the insulating gas pressure inside the model circuit breaker results in a higher maximum of mass flow, higher thermal conductance and higher withstand level as well as higher density as a factor of the convection but will reduce the wave velocity as another factor.

The nozzle affects the plasma in different ways: it results in a reduction of metal vapor content of an arc initiated by an exploding wire (advantage) if the optimum geometry (length and diameter) is selected but in general, it increases the arc temperature and changes the arc temperature distribution inside the nozzle (disadvantage).

There is a trade-off between the advantages/disadvantages of using a nozzle in the design of the model SCFCBs. Depending on the pressure and geometry, having a nozzle may fail in the recovery process as it increases T and the ablated copper from contacts cannot be easily dispersed in the dense SCF. From the current interruption point of view, there is probably no way around having a nozzle; hence the optimized geometry for the design pressure shall be numerically calculated through MHD simulations. Despite the low-pressure model CBs ($p < 7$ bar), the EEW is not a proper method for the study of SCFCBs due to stucking up the metal vapor in arcing area.

The gaseous discharges after wire explosion start at lower voltages than expected in a gas with the same temperature and metal content, due to UV radiation from the explosion and the exploding shocks which may have enough energy to ionize the gas in the expansion stage.

Acknowledgments

This work is supported by the Norwegian Research Council under Grant No. 280539.

ORCID iDs

A Kadivar https://orcid.org/0000-0002-4708-4438
F Abid https://orcid.org/0000-0001-8570-491X

References

[1] Chace W G and Moore H K 1964 *2nd Conf. on the Exploding Wire Phenomenon*
[2] Skryabin A S *et al* 2019 *J. Phys.: Conf. Ser.* **1250** 012018
[3] Taylor M J 2002 *J. Phys. D: Appl. Phys.* **35** 700
[4] Batra J, Jaiswar A C, Valvi R and Kaushik T C 2019 *IEEE Trans. Plasma Sci.* **47** 596
[5] Vijayan T and Rohatgi V K 1985 *IEEE Trans. Plasma Sci.* **13** 197
[6] Kadivar A and Niayesh K 2019 *J. Phys. D: Appl. Phys.* **52** 404003
[7] Cressault Y, Gleizes A and Riquel G 2012 *J. Phys. D: Appl. Phys.* **45** 265202
[8] Wu Y, Li M, Wu Y, Yang F and Guo P 2019 *Phys. Plasmas* **26** 43502
[9] Wang K *et al* 2017 *Chin. Phys. B* **26** 075204
[10] Yin G, Shi H, Fan Y, Wu J and Li X 2019 *J. Phys. D: Appl. Phys.* **52** 374002
[11] Aakervik J, Berg G and Hvidsten S 2011 *2011 Annual Report Conf. on Electrical Insulation and Dielectric Phenomena* pp 267
[12] Ezenwa I C, Secco R A, Yong W, Pozzo M and Alfè D 2017 *J. Phys. Chem. Solids.* **110** 386
[13] Maninger R C 1964 *3rd Conf. Exploding Wire Phenomenon* ed W G Chace and H K Moore (Boston, MA: Plenum Press)
[14] Keilhacker M 1960 *Z. Angew. Phys.* **12** (translation to be published by M Kilpatrick and F Webb)
[15] Koelman P M J *et al* 2016 *J. Phys.: Conf. Ser.* **682** 012034
[16] White G K and Collocott S J 1984 *J. Phys. Chem. Ref. Data* **13** 1251
[17] Chekhovskoi V Y, Tarasov V D and Gusev Y V 2000 *High Temp.* **38** 394
[18] Cahill J A and Kirshenbaum A D 1962 *J. Phys. Chem.* **66** 1080–2
[19] Tongxin Z, Makram E B and Girgis A A 1999 *IEEE Trans. Power Deliv.* **14** 1461
[20] Chul-Hwan K and Aggarwal R 2000 *Power Eng. J.* **14** 81
[21] Robertson D C, Camps O I, Mayer J S and Gish W B 1996 *IEEE Trans. Power Deliv.* **11** 1050
[22] Kadivar A and Niayesh K 2014 *Measurement* **55** 14
[23] Kadivar A and Sanaye-Pasand M 2005 *Power Eng. Conf. of Australasian Univ. (AUPEC)* Hobart, Tasmania
[24] Bennett F D, Kahl G D and Wedemeyer E H 1964 Ballistic Research Laboratories *Report* No. 1241
[25] Mott N F 1934 *Proc. R. Soc. A* **146** 465
[26] Reithel R J and Blackburn J H 1962 *A Hydrodynamic Explanation for the Anomalous Resistance of Exploding Wires* (Berlin: Springer)
[27] Abid F, Niayesh K, Jonsson E, Stoa-Aanensen N S and Runde M 2018 *IEEE Trans. Plasma Sci.* **46** 187
[28] Garanin S F and Kuznetsov S D 2009 *2009 IEEE Pulsed Power Conf.* p 697
[29] Haynes W M, Lide D R and Bruno T J 2015 *CRC Handbook of Chemistry and Physics* 96th edn (Boca Raton, FL: CRC Press)
[30] Sutton L E 1958 *Tables of Interatomic Distances and Configuration in Molecules and Ions* eds Bowen H J M, Sutton L E, Jenkin D G, Mitchell A D and Cross L C (London: Chemical Society) https://nla.gov.au/nla.cat-vn1006841
[31] Wong D S H, Orbey H and Sandler S I 1992 *Ind. Eng. Chem. Res.* **31** 2033
[32] Yexun L, Libing Y and Chengwei S 2003 *Plasma Sci. Technol.* **5** 1915
[33] Pletnev N V 2018 *Tech. Phys.* **63** 1137
[34] Vijayan T and Rohatgi V K 1988 *J. Appl. Phys.* **63** 2576
[35] Kadivar A and Niayesh K 2019 *5th Int. Conf. on Elec. Power Eq. Switching Tech* (Japan) (http://doi.org/10.1109/ICEPE-ST.2019.8928665)
[36] Chandler K M, Hammer D A, Sinars D B, Pikuz S A and Shelkovenko T A 2002 *IEEE Trans. Plasma Sci.* **30** 577
[37] Eichhoff D *et al* 2012 *J. Phys. D: Appl. Phys.* **45** 305204

[38] Godin D, Trépanier J Y, Reggio M, Zhang X D and Camarero R 2000 *J. Phys. D: Appl. Phys.* **33** 2583
[39] Abid F, Niayesh K and Støa-aanensen N 2019 *Plasma Phys. Technol.* **6** 23
[40] Malik N H 1981 *IEEE Trans. Electr. Insul.* **EI-16** 463
[41] Warne L K, Jorgenson R E and Nicolaysen S D 2003 Ionization coefficient approach to modeling breakdown in nonuniform geometries *Report* (Livermore, CA: Sandia National Laboratories, operated for the United States Department of Energy) (https://core.ac.uk/download/pdf/188996383.pdf)
[42] Korolev I U D and Mesiats G A 1993 *Physics of Pulsed Breakdown in Gases* (Yekaterinburg: Russian Academy of Sciences)
[43] Komuro A, Matsuyuki S and Ando A 2018 *Plasma Sources Sci. Technol.* **27** 105001
[44] Raizer Y P 1997 *Gas Discharge Physics* (Berlin: Springer)
[45] Hagelaar G and Pitchford L 2005 *Plasma Sources Sci. Technol.* **14** 722
[46] *SIGLO DataBase* 2013 edited by GREPHE (LXCat, LAPLACE, Toulouse, France) (http://www.lxcat.net/SIGLO)
[47] Chace W G and Moore H K 1961 *2nd Conf. on the Exploding Wire Phenomenon* (Berlin: Springer) (http://doi.org/10.1007/978-1-4684-7505-0)
[48] Bennett F D 1967 *Rev. Sci. Instrum.* **38** 293
[49] Zou X B, Mao Z G, Wang X X and Jiang W H 2012 *EPL* **97** 35004
[50] Abid F, Niayesh K, Espedal C and Støa-Aanensen N 2020 *J. Phys. D: Appl. Phys.* **53** 185503
[51] Zhou Q, Zhang Q, Zhang J, Zhao J, Ren B and Pang L 2011 *Plasma Sci. Technol.* **13** 661
[52] Cressault Y, Hannachi R, Teulet P, Gleizes A, Gonnet J-P and Battandier J-Y 2008 *Plasma Sources Sci. Technol.* **17** 035016
[53] Liu J *et al* 2016 *J. Phys. D: Appl. Phys.* **49** 435201
[54] Zhang B, Xiong J, Chen L, Li X and Murphy A B 2020 *J. Phys. D: Appl. Phys.* **53** 173001
[55] Kadivar A 2019 *34th Int. Power System Conf. (PSC-2019)* (IEEE, Tehran, Iran) (http://doi.org/10.1109/PSC49016.2019.9081479)
[56] Kadivar A and Niayesh K 2020 Effects of fast elongation on switching arcs characteristics in fast air switches *Energies* **13** 4846